Article:
Zhang, B, Yao, S, Wignall, PB orcid.org/0000-0003-0074-9129 et al. (3 more authors) (2019) New timing and geochemical constraints on the Capitanian (Middle Permian) extinction and environmental changes in deep-water settings: evidence from the Lower Yangtze region of South China. Journal of the Geological Society, 176 (3). pp. 588-608. ISSN 0016-7649

https://doi.org/10.1144/jgs2018-137

Accepted Manuscript

Journal of the Geological Society

New timing and geochemical constraints on the Capitanian (Middle Permian) extinction and environmental changes in deep-water settings: Evidence from the Lower Yangtze region of South China

Bolin Zhang, Suping Yao, Paul B. Wignall, Wenxuan Hu, Biao Liu & Yongle Ren

DOI: https://doi.org/10.1144/jgs2018-137

Received 8 July 2018
Revised 3 February 2019
Accepted 4 February 2019

New timing and geochemical constraints on the Capitanian (Middle Permian) extinction and environmental changes in deep-water settings: Evidence from the Lower Yangtze region of South China

Bolin Zhang[1], Suping Yao[1*], Paul B. Wignall[2], Wenxuan Hu[1], Biao Liu[1], Yongle Ren[1]

[1] *School of Earth Sciences and Engineering, Nanjing University, Nanjing 210023, China*

[2] *School of Earth and Environment, University of Leeds, Leeds LS2 9JT, UK*

**corresponding author: spyao@nju.edu.cn*

ABSTRACT: The Capitanian (Guadalupian) witnessed one of the major crises of the Phanerozoic and, like many other extinctions, it coincided with the eruption of large igneous province, in this case the Emeishan Traps of Southwest China. However, the timing and causal relationships of this event are in dispute. This study concentrates on the deep-water chert-mudstone strata of the Gufeng Formation and its transition to the Yinping Formation at Chaohu. Zircons from tuffs in the uppermost Gufeng Formation yield a U-Pb age of 261.6 ± 1.6 Ma, and comparison with sections around Emeishan suggests that they appeared in the *Jinogondolella altudaensis* conodont zone and persisted to the *Jinogondolella xuanhanensis* zone. This coincides with the Emeishan eruptions, and suggests that they probably derived from this province. Mineralogical and geochemical characteristics also show the tuffs are of acid volcanogenic origin and have a geochemical fingerprint of the ELIP. Our dating show that a crisis amongst radiolarians and a subsequent productivity decline occurred during the middle Capitanian, prior to the Guadalupian-Lopingian boundary. The Emeishan eruptions began immediately before this, indicating a likely causal relationship between these events. Major regression and marine anoxia/euxinia are two other important extinction-relevant environmental changes that occurred during this critical interval.

The late Guadalupian crisis was of comparable magnitude to other mass extinctions (e.g., end-Triassic or end-Ordovician, Stanley and Yang 1994; Clapham et al. 2009; Wignall 2015; Stanley et al.,

2016) with nearly 62 % species and 34 % marine genera extinction (Stanley et al., 2016) and was originally named the "Guadalupian-Lopingian boundary (G-LB) event" (Stanley and Yang 1994) and is now more often known as the Capitanian mass extinction (Bond et al. 2010a). It is considered to mark the start of the Paleozoic-Mesozoic transition in the marine realm (Isozaki 2009b; Bond et al. 2015). The age of the crisis is currently debated with estimates ranging from the Wordian-Capitanian transition (Gand and Durand 2006; Lucas 2009; Shen and Shi 2009; Groves and Wang 2013) to the early Lopingian (Nielsen and Shen 2004; Kaiho et al. 2005), with most favouring either an end-Guadalupian (end-Capitanian, Wang and Sugiyama 2000; Leven 2003; Yang et al. 2004; Retallack et al. 2006; Isozaki 2009a,b) or mid-Capitanian (Wignall et al. 2009a; Bond et al. 2010a,b; De la Horra et al. 2012; Wignall et al. 2012; Isozaki & Servais, 2018) age. In order to be consistent and clear in the following text, from herein we refer to this event as the ''Capitanian mass extinction''.

The cause of the Capitanian mass extinction is equally debated with several mechanisms proposed: regression and consequent shallow-marine habitat loss (e.g., Jin et al. 1994; Shen and Shi 2002; Clapham et al. 2009; Bond and Wignall 2009; Wignall et al. 2009b), explosive eruptions of the Emeishan large igneous province (ELIP, e.g., Ali et al. 2002; Zhou et al. 2002; He et al. 2007; Wignall et al. 2009a; Bond et al. 2010b; Huang et al., 2019), oceanic anoxia (e.g., Isozaki 1997; Saitoh et al. 2013a,b; Yan et al. 2013; Saitoh et al. 2014; Bond et al. 2015; Zhang et al. 2015) a proposed end-Capitanian cooling phase known as the Kamura event (e.g. Isozaki et al. 2007).

Previous stratigraphic research on the Capitanian mass extinction event focused on fossiliferous, shallow marine Tethyan carbonates (e.g. Penglaitan and Tieqiao sections; Wang et al. 2004; Shen et al. 2007; Shen and Shi 2009; Zhang et al. 2015), the mid-superocean Panthalassa (e.g., Gujohachiman and Kamura sections, Japan; Ota and Isozaki 2006; Isozaki et al. 2007; Wignall et al. 2010; Nishikane et al.

2014) and mid-high latitude, Boreal shelf sections (Bond et al. 2015). The study of this interval is hindered by the major regression in the late Guadalupian (Haq and Schutter 2008; Wignall et al. 2009b), which resulted in worldwide erosion and the development of unconformities on shelves and platforms (Jin et al. 2006; Wignall et al. 2012). Consequently, many sections have a major hiatus around the key extinction level (e.g., Ota and Isozaki 2006; He et al. 2007; Lai et al. 2008; Saitoh et al. 2013a; Yuan et al. 2017). In addition, a proposed pre-eruptive crustal uplift of the ELIP likely promoted increased weathering and erosion rates (Hu 1993; He et al. 2003, 2009). In contrast, the deep-water slope/basin facies offer more complete sedimentary records due to their greater water depth and can preserve a more detailed record of events at this time.

During the Guadalupian, a biostratigraphically complete, deep-water slope/basin succession with bedded chert-mudstone sequences was deposited on the northern margin of the Yangtze platform in South China. However, due to poor biostratigraphic resolution and lack of precise geochronological ages for stratigraphic boundaries, research on the Capitanian mass extinction event in this region is limited. Fortunately, due to recent mining and excavation, we have been able to study a relatively complete, newly exposed Guadalupian section at Pingdingshan, Chaohu City, Anhui Province.

In this paper, we present a multidisciplinary study that includes stratigraphic, palaeontological, geochronological and geochemical data from the Pingdingshan section in order to evaluate the horizon of the Capitanian mass extinction and related geological events (ELIP eruption, regression and marine anoxia), enable comparison with other sections around the world and discuss kill mechanisms.

Geological setting

Palaeogeographic setting

As a large northeast-southwest trending carbonate platform, the Yangtze area in South China was

located in the equatorial eastern Paleo-Tethys Ocean (Enkin et al. 1992; Wang and Jin 2000) and is postulated to have experienced intensive, periodic trade wind upwelling during the Guadalupian (Kametaka et al. 2005; Yao et al. 2015; Zhang et al., 2018) (Fig. 1a). The chert-mudstone rhythms of the Gufeng Formation accumulated in widespread, deep-water shelf basins in the northern and southern margins of the Yangtze Platform, and were laterally equivalent to the carbonate-dominated Maokou Formation on the platform (Fig. 1b). The Chaohu area was in a transition zone on the northern outer shelf of the Yangtze Platform (Kametaka et al. 2005, 2009; Fig. 1b). In the late Guadalupian, a large-scale regression led to shallow water deposition in the lower Yangtze area recorded by the Yinping Formation. This shallowing coincides with a huge decline in benthos and plankton, leaving only small bivalves, brachiopods and ammonoids (Bureau of Geology and Mineral Resources of Anhui Province 1989).

Stratigraphy and Chronology

Guadalupian strata are mainly composed of the Gufeng (Kuhfeng) Formation and Yinping Formation. The Gufeng Formation unconformably overlies the shallow-marine limestones of the Qixia (Chihsia) Formation and is composed of bedded, black chert, siliceous mudstone and carbonaceous mudstone. It is subdivided into three members: Lower Phosphate Nodule-bearing Mudstone Member (LPMM), Middle Chert-Mudstone Member (MCMM) and Upper Mudstone Member (UMM) (Wu et al. 2015). The Gufeng Formation contains abundant fossils, including radiolaria, sponge spicules, ammonoids, bivalves, brachiopods and conodonts (Jin and Hu 1978; Zhao et al. 1983; Bureau of Geology and Mineral Resources of Anhui Province 1989; Kametaka et al. 2009; Ito et al. 2013). Three regional radiolarian assemblage zones, spanning the Roadian-Capitanian stages, have been established in the Gufeng Formation of the Chaohu area (Kametaka et al. 2009; Ito et al. 2013), and deposition may have spanned at least 4.7 Myr (Yao et al. 2015). The overlying Yinping Formation consists of shallow-water black to pale-grey mudstone,

shale and siltstone with trace fossils (Bureau of Geology and Mineral Resources of Anhui Province 1989) and is, in turn, succeeded by the Longtan sandstone. *Neomisellina* fusulinids in the Yinping Formation indicate a late Capitanian age (Kametaka et al. 2009), but more precise biostratigraphic dating is needed.

Study section

The study section is located on the north limb of the Pingdingshan syncline in the Chaohu area (GPS 31°37′51.5″ N, 117°49′21.8″ E) and contains a complete Permian section (Fig. 1c, d). As reported in Kametaka et al. (2005), the Gufeng Formation of this study section is approximately 31 m thick and its three members can be recognized (Fig. 2). Of the Yinping Formation, only its lower shale member (LSM, Fig. 2) is well exposed along with parts of the middle and upper members (MSM and USM). Here we focus on the transition from the Gufeng to Yinping Formations (the upper MCMM, UMM, LSM and lower MSM).

Samples and analytical methods

A total of 102 chert, mudstone and shale samples, and 11 tuff samples were collected from the Upper Gufeng Formation and the Lower-Middle Yinping Formation of the Pingdingshan section. Despite attempts to preferentially collect unweathered rock samples, some tuffs show weathering to varying degrees as evidenced by the presence of white to light grey soft clay. These weathered surfaces and visible post-depositional veins were trimmed off, each sample was cut into small chips and pulverized to ~ 200 mesh size in an agate mortar.

To determine the age of the tuffs, two samples (CH-3, PDS-5) from the top of the Gufeng Formation were selected for zircon U-Pb dating. The zircons were separated using conventional magnetic and density techniques to concentrate the non-magnetic, heavy fractions and were then mounted in epoxy resin and polished to expose the grain centres. The cathodoluminescence (CL) photos and zircon U-Pb isotopes were analyzed at the State Key Laboratory for Mineral Deposits Research, Nanjing University. The

CL photos were acquired using a Mono CL4 (Gatan, U.S.A.) attached to a field emission scanning electron microscope (Carl Zeiss Supra 55). The zircon U-Pb isotopes were analyzed using an Agilent 7500a ICP-MS attached to a New Wave 213 nm laser ablation system with an in-house sample cell. The U-Pb ages were calculated from the raw signal data using the on-line software package GLITTER (ver. 4.4). The detailed analytical procedures were similar to those described by Griffin et al. (2004) and Jackson et al. (2004). Because ^{204}Pb could not be measured due to its low signal and interference from ^{204}Hg in the gas supply, a common lead correction was carried out using the EXCEL program ComPbCorr#3_15G (Andersen 2002). The LA-ICP-MS U-Pb isotopic data are listed in Table 1. All of the U-Th-Pb age calculations and concordia diagram plots were made using the ISOPLOT program (ver. 3.76) of Ludwig (2012).

Both the TOC and TS contents analyses were performed via combustion using an Elementar® Vario MACRO CHNS elemental analyzer at the Key Laboratory of Surficial Geochemistry of the Ministry of Education, with errors less than 1% and 5%, respectively. The samples were treated with 2 N HCl for 24 h to remove inorganic carbon, washed to neutral and dried for the final test on the machine. The identified bulk minerals and compositions of the major and trace elements of the tuffs were analyzed at the State Key Laboratory for Mineral Deposits Research, Nanjing University. The identification of bulk minerals was carried out on unoriented powder mounts by X-ray diffraction (XRD) using a Rigaku Rapid II X-ray diffraction system with a Mo target X-ray source and a 0.3 mm diameter beam. The major element concentrations were determined by wavelength-dispersive X-ray fluorescence spectrometry techniques (ARL9900 XRF) with an analytical precision of ± 1% for sample concentrations larger than 1.0 wt.% and ± 10% for sample concentrations less than 1.0 wt.%. Loss on ignition (LOI) was calculated by the difference values of samples burned in a muffle at 1050 °C for 2 h. The trace elements were measured using a Finnigan Element 2 high-resolution inductively coupled plasma mass spectrometer (HR-ICP-MS) with an

analytical error of less than 5%.

Results

Lithology and mineralogy

The upper MCMM is primarily composed of alternating beds of thin black chert, less than 10 cm thick, and brown, siliceous mudstone (Fig. 3a, c, d) with dozens of interbedded grey tuffs (Fig. 3c-e). The proportion of siliceous mudstone increases in the upper part of the MCMM. Petrographic examination of the chert shows that the composition is dominated by chalcedonic quartz, radiolarians and their debris (Fig. 4a). The matrix has contents of 20-30% and mainly consists of cryptocrystalline quartz and black organic matter, with small amounts of clay minerals. The thinly bedded siliceous mudstone is mainly composed of clay minerals, with a few radiolarians, and shows a compacted fabric but no lamination (Fig. 4b). The interbedded tuff occurs as grey to light grey thin beds with average thicknesses of 0.5 - 1 cm (Fig. 3 c-e, j). They are very fine grained and show sharp contacts with the overlying and underlying rock layers. In the UMM, the well-bedded, chert-mudstone sequences are replaced by poorly fossiliferous, carbonaceous mudstones (Fig. 3b, f) interbedded with grey tuffs. The tuff used for dating at the top of the UMM is approximately 7 cm thick (Fig. 3g, j). Detailed microscopic observations show that the tuff is composed of quartz, feldspar, zircon and muscovite grains in a clay mineral-rich matrix (Fig. 4c-e). The quartz consists of both corroded and embayed grains and euhedral, hexagonal bipyramidal crystals (Fig. 4d-e).

The LSM is mainly well-bedded, grey to grey-black, pyritic shale interbedded with grey mudstone (Fig. 3h), whereas the MSM only consists of grey shale. The shales contain small, inflated bivalves (often packed in layers), ostracods and other fossils (Fig. 4g-i). The upper Yinping Formation is a greyish yellow silty mudstone interbedded with sideritic siltstone and siliceous nodules and has the same fauna albeit

much rarer (Fig. 4f). The lithological disconformity between the silty mudstone of the Yinping Formation and the overlying sandstone of the Longtan Formation (Fig. 3k) is considered to be the possible G-LB in the Lower Yangtze area (Bureau of Geology and Mineral Resources of Anhui Province 1989).

Radiolarian palaeontology

The record of microfossil abundance and evolutionary lineages of radiolarians in the Gufeng and Yinping formations is shown in figure 2 and is based on previous studies (e.g., Wang and Qi, 1995; He et al., 1999; Kametaka et al., 2009; Wang and Yang, 2011). Radiolarians are the most abundant microfossil in the Gufeng Formation, especially in the MCMM. The deeper dwelling Albaillellaria are abundant in the lower MCMM but decreases upward, whereas Entactinaria and Spumellaria, which inhabited relatively shallower waters, dominate the middle-upper MCMM (Fig. 2).

Three radiolarian assemblage zones have been established: the *Pseudoalbaillella (P.) longtanensis –P. fusiformis* (Roadian-Wordian), *Follicucullus (F.) monacanthus* (Wordian-early Capitanian), and *F. scholasticus–Ruzhencevispongus uralicus* zones (early-middle Capitanian) (Wang and Qi, 1995; Kametaka et al., 2009; Fig. 2). These reflect the evolutionary clades of *Pseudoalbaillella* and *Follicucullus*: the *P. ishigai-P. fusiformis-P. monacanthus* lineage and the *F. scholasticus-F. porrectus-F. ventricosus-F. charveti* lineage (Wang and Yang, 2011).

The UMM, a black carbonaceous mudstone, is barren of fossils (Fig. 2), which do not return until the grey shales at the bottom of the LSM (~0.5 m above the dated tuff) where small bivalves, brachiopods and ostracods occur concentrated in layers (Fig. 2, Fig. 4 f - i).

Zircon U-Pb dating

Zircon CL images and the results of U-Pb isotopic analyses from the Pingdingshan section are presented in figure 5. The zircons are clear, pale, euhedral crystals with well-developed tetragonal

dipyramids and magmatogenic oscillatory zoning, which suggest a typical igneous origin. This is further supported by their relatively high Th/U ratios (0.52-1.30), which had U contents of 89.7-613.7 ppm and Th contents of 55.7-528.5 ppm (Table 1). The Th/U ratios of the magmatogenic zircon grains normally exceeded 0.4 (Belousova et al. 2002; Rubatto 2002). These zircons are well suited for dating analyses (Wu et al. 2004). Spreading along the concordia line, both samples (CH-3 and PDS-5) yielded weighted mean $^{206}Pb/^{238}U$ ages of 261.6 ± 1.6 Ma (MSWD = 0.37) and 261.5 ± 1.6 Ma (MSWD = 0.84), respectively. These ages represent the crystallization age of the zircons and the corresponding eruption time of the tuffs, which also can be used to limit the stratigraphic boundary age of the Gufeng and Yinping Formations.

XRD results

Representative XRD diagrams are shown in figure 6. The XRD data indicate that most of the tuffs have been altered into clay minerals, which are mainly composed of illite, illite-smectite mixed-layers (I/S) and kaolinite, and also contain quartz, muscovite and zircon. In the clay fraction of the tuff layers, the major component is an illite-smectite mixed-layer (I/S), which is typical of most Paleozoic K-bentonites, which are a diagenetic product of smectite alteration. Under a moderate to high intensity of diagenesis, the smectite-rich claystones would also have gradually transformed to interstratified I/S and illite, and some would have been altered to kaolinite. Quartz and zircon with contents of less than 5% indicate that the tuff can be derived from airborne acid volcanic ash (e.g., He et al., 2010, 2014; Fang et al., 2016; Liao et al., 2016).

Major elements

The major elemental compositions of the tuffs in the Pingdingshan section are listed in Table 2. All of the samples had high LOI values of 9.8-13.15 wt.%, which is consistent with the high percentage of clay minerals in these rocks. The bulk rock analyses were characterized by high Al_2O_3 (26.51-37.42 wt.%) and

low total alkali (K_2O + Na_2O) contents (0.93-3.54 wt.%). With an average value of 51.55 wt.%, the relatively stable SiO_2 content had a strong negative correlation with Al_2O_3, indicating that the SiO_2 had experienced losses during weathering. Due to the relatively low contents of TiO_2 (0.126-0.41 wt.%), the high Al_2O_3/TiO_2 ratios (65-270) were greater than the values of the tuff and its altered compositions (~40, Zhang et al. 2005), also suggesting a volcanic origin.

Trace elements

The analytical results of the trace elements and relevant parameters are given in Table 2. The primitive-mantle-normalized trace element patterns of the tuffs (Fig. 7) display positive anomalies of large ion lithophile elements (e.g., Rb, Th, U and Pb) and negative anomalies of high field strength elements (e.g., Nb, Zr and Ti). In addition, a significant negative Ba anomaly was observed. Rare earth elements are useful for tracing diagenetic processes and are commonly used to distinguish lithological features (Rollinson 1993). The total rare earth element (∑REE) concentrations of the samples vary from 41.5 to 610.5 ppm, with a mean value of 242 ppm. All the samples show pronounced negative Eu anomalies (δEu = 0.41–0.60, mean = 0.48) and weak Ce anomalies (δCe = 0.88–1.12, mean = 1.00). In the chondrite normalized REE distribution patterns (Fig. 8), all the samples have typical fractionated patterns, strong enrichments of light rare earth elements (LREEs) and a relatively weak, fractionated flat pattern of heavy rare earth elements (HREEs).

TOC and TS

The total organic carbon (TOC) and total sulfur (TS) contents of the 102 samples are shown in Table 3 and figure 2. The Gufeng Formation samples have extremely high TOC contents (2.46 - 27.56 wt.%, mean 13.82 wt.%) and relatively low TS contents (0.26-3.54 wt.%, mean 1.07 wt.%). The LSM of the Yinping Formation shows upward decrease of TOC contents from 17.47 wt.% to 0.88 wt.%, whilst TS contents are

higher than seen in the underlying Gufeng Formation and range from 2.54 wt.% to 10.31 wt.%. The lower MSM is characterized by relatively low TOC contents (mean 0.95 wt.%) and TS contents (mean 0.36 wt.%). The positive correlation between TOC and TS of the MCMM and the UMM (Fig. 9) indicates a marine depositional environment where the intensity of sulfate reduction is dependent on the availability and abundance of metabolizable organic matter (Berner 1984; Berner and Raiswell 1984). The TS content of LSM increase significantly, yielding no correlation with TOC (Fig. 9), which suggests a main sulfide source for TS (Fig. 2). In addition, both the MCMM and the UMM have low TS/TOC ratios, which ranging from 0.03 to 0.16 and had a mean of 0.07, whereas the LSM had high TS/TOC ratios that ranging from 0.2 to 4.85 and had a mean of 2.37 (Fig. 2). The lower MSM have relatively consistent TS/TOC ratios (mean 0.39) with modern marine environment (~0.36, Berner and Raiswell 1984).

Discussion

Volcanic activity of the ELIP

Geochronology significance of the tuffs

The temporal relationship between the onset of ELIP volcanic activity and Capitanian extinction losses is well established and began at least two conodont zones prior to the G-LB in the *Jinogondolella (J.) altudaensis* zone (~263 Ma, Sun et al. 2010) of the mid-Captianian (Wignall et al. 2009a; Bond et al. 2010b). The eruptions became more extensive and large-scale in the *J. xuanhanensis* zone (~262 Ma, Sun et al. 2010, Fig. 10). Based on the high-resolution floating point time scale of the Capitanian Stage established at the Tieqiao section, Xue et al. (2015) estimated that the onset and peak of the ELIP eruptions occurred at ~262.67 Ma (at the top of *J. altudaensis* zone) and at 261.86 Ma (*J. xuanhanensis* zone, Fig. 10), respectively. In this study, the $^{206}Pb/^{238}U$ ages of the two tuffs at the top of the Gufeng Formation were 261.6 ± 1.6 Ma and 261.5 ± 1.6 Ma and so are concordant with the reported eruption

time of the ELIP (262~259Ma; He et al. 2007, 2010; Xu et al. 2008; Wignall et al. 2009a; Zheng et al. 2010; Zhong et al. 2014) and are probably close to its peak. It is noteworthy that the upper part of MCMM also has numerous tuff horizons (Fig. 2, 11), which occurred prior to 261.6 ± 1.6 Ma. The dated tuff at the top of the UMM (~7 cm thick) is the thickest example and so could tentatively be regarded as a record of peak volcanism.

The Milankovitch cyclostratigraphy, recorded by the chert-mudstone couplets of the Gufeng Formation, indicates an average sedimentation rate of 4.8 m/Ma in the Chaohu region during the Guadalupian (Yao et al. 2015). Given stable sedimentation rates, this indicates that the tuffs of the upper Gufeng Formation formed over ~2 Myr. Using a top tuff age of 261.6 Ma as a baseline, we further estimate that the onset time of the tuffs was approximately in the *J. altudaensis* zone, which is in accordance with the beginning time of the ELIP eruption seen in south-west China (Wignall et al. 2009a).

In addition to the basaltic volcanic rocks, many sections (e.g., Pingdi, Qingyin, and Xiongjiachang) within the ELIP were also found to have multiple layers of grey and white volcanic ash (Fig. 10) in their middle-late Capitanian strata (Bond et al. 2010b; Sun et al. 2010). The Guadalupian-Lopingian boundary stratotype at the Penglaitan section near the ELIP margin also has thin pale cream ash beds interbedded with cherts below the Laibin Limestone and sand-grade pyroclastic debris in the Laibin Limestone (Wignall et al. 2009b). Such common and widely distributed ash beds and pyroclasts indicate an unusually violent eruptive style for the ELIP that was capable of lofting them a considerable distance (Wignall et al. 2009a).

Based on the studies of high-resolution biostratigraphy of conodonts, lithostratigraphy and chronostratigraphy in South China (Fig. 10), we compared the Pingdingshan section with sections near the ELIP and found that the tuffs first appeared in the *J. altudaensis* zone and consistently continued to the *J. xuanhanensis* zone, whereas the volcanic debris first appeared in the basal part of the *J. granti* zone

(Penglaitan Section) and continued to the earlier *C. postbitteri* zone (Tieqiao Section) (Wignall et al. 2009a). These findings suggest that the volcanic products have a temporal link and are likely to be sourced from the eruption of the ELIP (*J. altudaensis* zone to *J. granti* zone, Sun et al. 2010; Zhong et al., 2013).

Volcanogenic origin of the tuffs

According to their mineralogical characteristics, the tuffs in the upper Gufeng Formation have an acid volcanogenic origin. Bona fide air-borne tuffs generally contain illite and montmorillonites with 1-10% quartz (Altaner and Grim 1990; Zhou 1999). Therefore, the high contents of illite, illite-smectite mixed-layers (I/S) and kaolinite with relatively low contents of quartz, muscovite and zircon (less than 5%) shown by the XRD results and microscopic observations indicate that our samples are typical acid tuffs or volcanic ashes. These illite, illite-smectite mixed-layers (I/S) and kaolinite are thought to be originated from the diagenetic alteration of volcanic breccia sediments or volcanic ash. In addition, large amounts of high temperature quartz (β quartz and angular quartz) are characteristic of felsic tuff (e.g., Zhang et al. 2007). Fine crystallographic hexagonal double cone-like high-temperature β-quartz, such as found in our samples (Fig. 4e), is the typical product of the rapid condensation of acid volcanic eruptions. The angular quartz grains, including corroded and embayed examples, may have been formed due to the influence of high-temperature volcanism. The volcanogenic origin is further confirmed by the euhedral zircons with well-developed tetragonal dipyramids and magmatogenic oscillatory zoning (Fig. 5), which yielded uniform ages.

Integrated analysis of geochemical proxies also helps determine the source of the tuffs. First, the Al_2O_3/TiO_2 ratio remains virtually constant during surface weathering, hydrothermal alteration and volcanic process (i.e., from volcanic eruption to ash-deposition) (Zhou 1999; He et al. 2010) and is the

most useful indicator for the provenance of sedimentary rocks (Taylor and McLennan 1985) and acid tuffs (Zhou and Kyte 1988). For acidic tuffs and their alteration products, the ratio is typically greater than 40 (Spears and Kanaris-Sotiriou 1979; Zhou et al. 1982) and so the relatively high Al_2O_3/TiO_2 ratios of all the samples, which ranged from 65 to 270, indicates they are acidic tuff (Spears and Kanaris-Sotiriou 1979; Zhou et al. 1982; Zhou and Kyte 1988; Zho, 1999). Second, the TiO_2 (wt.%)-Al_2O_3 (wt.%) bivariate diagram (Fig. 11a), which is widely used to determine the compositions of source rocks (McLennan et al. 1980), also shows its felsic characteristics, which indicate a felsic ELIP source. In addition, it can be seen from the Zr/TiO_2-Nb/Y diagram (Fig. 11b) that, with the exception of one sample falling in the trachyandesite field due to the migration of Y in the process of alteration into clay minerals (Christidis 1998), almost all of the samples are rhyodacite-rhyolites. Third, the Th-Co diagram effectively identifies altered and strongly weathered volcanic and volcanic clastic rocks (Hastie et Al. 2007; Eyuboglu 2015). With the exception of one sample, the samples plot within the high-K calc-alkaline and shoshonite series of rocks (Fig. 11c) due to their high Th contents (7.3-47.8 ppm) and the dacite-rhyodacite series of rocks due to their lower Co contents (0.8-2.7 ppm). Finally, with the exception of CH-ash-8 (651.72), the Ti/Th ratios (24.13-199.89) of the samples were approximately the same as those of acid volcanic rocks (30-400). The higher concentrations of both Th (mean 23.4 ppm) and U (mean 9.6 ppm) also suggest an acidic or felsic origin (e.g., Liao et al., 2016). In addition, the typical fractionated and strong enrichment of LREEs and the relatively weak fractionated flat pattern of HREEs with strong Eu negative anomalies (δEu = 0.41-0.60, mean 0.48) also show that these tuffs have a felsic origin (Fig. 8).

Possible relationship of tuffs with the ELIP

Although the loss of movable elements may result from strong tuff alteration, stable elements (e.g., Zr, Hf, Nb, Ta, Th, U, Y, Sc, REY) usually remain constant and are useful for determining the sources of

volcanic ash (e.g. Spears and Kanaris-sotiriou 1979; Zhou 1999; Spears 2012). In the K_2O-SiO_2 discrimination diagrams (Fig. 11d), all of the samples fell within the field of the calc-alkaline to high-K calc-alkaline series of volcanic rocks, suggesting that they are relatively rich in potassium and may show both crustal and mantle geochemical features. The chondrite-normalized REE distribution pattern diagram (Fig. 8) and primitive-mantle-normalized trace element spider diagram (Fig. 7) also show strong depletions of Eu, Nb, Ba, P, Sr and Ti, and remarkable enrichments of LREE, Th, U and Pb, which indicate that the formation of the tuffs may have been affected by the assimilation of crustal materials (Anh et al. 2011; Ernst 2014). This may suggest a similar source with the Emeishan silicic volcanic rocks, which were formed by fractional crystallization-dominated magmatic processes from basaltic parent magmas with crustal assimilation (Shellnutt and Jahn 2010; Xu et al. 2010; Yang et al. 2015). In addition, the peraluminous feature, as indicated by high Al_2O_3 but low $K_2O + Na_2O$ and CaO contents, may be related to the contamination of small amounts of crustal melts (Anh et al., 2011). All of the above data suggest that these acidic felsic tuffs were produced from a lithospheric mantle that was contaminated by crustal material. This result is compatible with previous studies made on the silicic volcanic rocks in the ELIP (Shellnutt and Jahn 2010; Xu et al. 2010). Furthermore, in the Hf-(Rb/10)-(Ta×3) and Hf-(Rb/30)-(Ta×3) tectonic discrimination diagrams (Fig. 12), most of the tuffs fall in the WPG field, which is consistent with the tectonic background of the ELIP. Previous studies suggest that tuffs, with these characteristics, could also be derived from subduction-zone volcanic arcs around the South China Block during the Middle Permian (e.g., Li et al., 2006; Zhong et al., 2013). However, such sources were considerable distances from the study area (>1200 km) making such sources unlikely. Instead, we suggest that our studied tuffs are probably derived from the ELIP.

The mid-Capitanian biotic crisis

The Capitanian crisis was first identified from a literature meta-analysis that showed major extinctions in the Guadalupian that were assumed to have happened at the end of this series (Jin et al. 1994; Stanley and Yang 1994). However, subsequent research on biostratigraphically constrained sections in SW China showed that the losses occurred within the *J. altudaensis-J. prexuanhanensis* conodonts zone of the mid-Capitanian Stage, and coincided with the onset of the ELIP volcanic activity significantly before the G-LB (Wignall et al. 2009a; Bond et al. 2010b; Wignall et al. 2012; Wignall 2015). Fossil records from the Tieqiao and Penglaitan sections of SE China indicate a slightly younger extinction age beginning in the *J. xuanhanensis* zone to the G-LB (Jin et al. 1994, 2006; Mei et al. 1998; Shen and Shi 2009; Wang and Sugiyama 2000).

A possible biotic crisis of radiolarian?

The chert-mudstone rhythmic sequence of the Pingdingshan section is rich in radiolarian fossils, and three radiolarian assemblage zones were established (e.g., Wang and Qi, 1995; He et al., 1999; Kametaka et al., 2009; Ito et al., 2013; Fig. 2). Study of their record in the Gufeng Formation at Chaohu (e.g., Kametaka et al. 2009), shows that the abundance of radiolarians does not change greatly from the bottom to top, but all died out abruptly coincidental with the disappearance of chert at the end of the MCMM (Fig. 2). Our dating shows this level is within the Capitanian and coincides with ELIP volcanism (Fig. 2 and 10). A similar rapid decline in the abundance of radiolarian also occurred in the Maocaojie (Shi et al. 2016) and Luojiaba (Ma and Feng, 2012; Ma et al., 2016) section of the Middle Yangtze. In addition, spumellarians in the *F. scholasticus* zone of the Luojiaba section also declined in average body size (Ma and Feng, 2012). Despite the lack of a precise lithological and biostratigraphical correlation with the Chaohu area, the broadly concurrent decreases indicate that radiolarians of the Paleo-Tethys Ocean

experienced a serious and regional crisis within the mid-Capitanian, which led to absence radiolarians in the *F.bipartitus*—*F.charveti* zone during the upper Capitanian strata (e.g., He et al., 1999; Kametaka et al., 2009; Ma and Feng, 2012; Ito et al., 2013; Shi et al., 2016; Ma et al., 2016).

A radiolarian biotic crisis likely also had occurred in the Panthalassa Ocean (e.g., Japan) and its periphery (e.g., west Texas of USA and Guangxi area of South China) somewhat later albeit still before the G-LB. In the Panthalassa sections of Japan, radiolarians experienced rapid turnover during the Capitanian (Isozaki, 2009b). *Pseudoalbaillella,* a long-lived genus that diversified and dominated in the Late Carboniferous to Middle Permian, became relatively smaller in body size and less abundant in the *Follicucullus monacanthus* zone (Isozaki, 2009b), and then experienced global extinction before the G-LB (Wang and Yang, 2011). *Follicucullus*, a dominant genus that appeared in the Capitanian (Isozaki, 2009b; Wang and Yang, 2011; Ito et al., 2016; Xiao et al., 2018), also became less dominant at the end of the Capitanian but survived into the Lopingian (Isozaki, 2009b). In west Texas (USA), these Middle Permian radiolarians all disappeared before the end Capitanian (e.g., Nestell and Nestell, 2010). In the Dachongling section of Guangxi area, albaillellarian (e.g., *Follicucullus* spp.) diversity and abundance clearly decreased in the uppermost part of the *F.charveti* Zone (Sun and Xia, et al., 2006). Although *Albaillella* spp. (e.g., *Albaillella cavitata*) occurred after a quiet of time, their abundance was still low (Sun and Xia, 2006). In addition, *Follicucullus* also shows faster turnover speeds in the Capitanian (*F. scholasticus-F. porrectus-F. ventricosus-F. charveti*) than other stage of the Permian (Xiao et al., 2018), suggesting possibly rapid environmental changes. In summary, we speculate that a global radiolarian biotic crisis could have occurred in both Panthalassa Ocean and Paleo-Tethys Ocean during the middle-late Capitanian.

Collapse of high primary productivity

The radiolarian crisis occurs during a phase of exceptionally high organic carbon accumulation (mean 15.1 wt.% TOC in the upper MCMM and mean 18.8 wt.% TOC in the UMM). Similarly high organic enrichment has also been reported in the Upper (e.g., the Shangsi section, Saitoh et al. 2013) and Middle (e.g., the Maocaojie section, Shi et al. 2016) Yangtze region. This suggests that there was no productivity collapse linked with the radiolarian crisis. The abrupt decline of TOC occurs during the transition to the Yinping Formation indicates a possible collapse of this high primary productivity. It is noteworthy that more powerful volcanisms, as indicated by the 7 cm boundary tuffs, predated this productivity collapse, which suggests a possible causal relationship between them.

The fossil content of the grey shales at the bottom of the LSM is mainly composed of small bivalves and ostracods (Zhao et al. 1983; Fig. 2), which are similar to the post-extinction survival communities seen after the Permo-Triassic mass extinction (Isozaki 2009b). The impoverished benthic fauna may reflect oxygen-poor conditions, as implied by the high TS contents and TS/TOC ratio. Furthermore, the relatively low TOC contents (mean 0.95 wt. %, Fig. 2) of the lower MSM suggest that a relatively low productivity was sustained in the aftermath of the extinction.

The mid-Capitanian Regression

The Guadalupian-Lopingian transition has long been recognized as a first-order eustatic lowstand, (Ross and Ross 1985; Hallam and Wignall 1999; Haq and Schutter 2008). More recent work indicates this regression likely occurred somewhat before the boundary in the early *J. xuanhanensis* zone in South China, as well as in Texas and Pakistan (Fig. 10) (Bond et al. 2010a; Sun et al. 2010), and probably also in Greece (Wignall et al. 2012). Thus, regression and consequent loss of shallow-marine habitat is a popular mechanism for the Capitanian mass extinction (e.g., Jin et al. 1994; Hallam and Wignall 1997, 1999; Wang

and Sugiyama 2000; Shen and Shi 2002; Yang et al. 2004; Bond and Wignall 2009).

A major regressive episode is also seen in the Lower Yangtze area at the sharp transition from the deep-water, basinal Gufeng Formation to the shallower mudstones and siltstones of the Yinping Formations. The dated boundary tuff has a relatively precise age of 261.6 ± 1.6 Ma, which indicates it is probably very close in age to the base of the *J. xuanhanensis* zone (Fig. 10). This regression was slightly later than the episodic volcanic activity of the ELIP and may have occurred when it was close to its peak, which is consistent with findings of Sun et al. (2010). In addition, the decrease and/or disappearance of radiolarian occurred earlier than the great regression in the east margin of the Paleo-Tethys Ocean during the middle Capitanian, which can be confirmed in both Chaohu and Maocaojie section (Shi et al., 2016). This indicates that facies change may not be the main cause of radiolarian disappearance (e.g., Kuwahara et al., 2007; Kametaka et al., 2009; Ito et al., 2013). Thus, the regression occurred after the radiolarian turnover which supports the viewpoint of Bond et al. (2010a) that it is younger than the extinction event (in the *J. altudaensis* Zone). Therefore, the regression is unlikely to have triggered the biotic crisis (Bond et al. 2010a).

The mid-Capitanian marine anoxia

Redox conditions

Based on sedimentological and geochemical evidence, Kametaka et al. (2005) argued that the Gufeng Formation was deposited mainly on a suboxic-anoxic outer continental shelf with an oxygen minimum zone (OMZ) developed at intermediate water depths. The depletion of TS in comparison to high TOC values is an attribute seen in modern sediments beneath high-productivity upwelling regions (Morse and Emeis 1990; Smolarek et al. 2017) but not for sediments from normal marine depositional conditions (Berner and Raiswell 1984; Smolarek et al. 2017). Therefore, the higher TOC and lower TS in the MCMM

(Fig. 2) indicate an anaerobic-anoxic seawater column with a more regularly ventilated seafloor, whereas the relatively increased TS and TOC in the UMM (Fig. 2) suggest increased sulfide deposition and a relatively anoxic water column. In the LSM, the extremely high TS contents with lower TOC contents indicate an anoxic/euxinic marine environment, although the presence of bivalves and ostracods point to brief oxygenation events.

The TS/TOC ratio is also commonly used as a palaeoredox proxy (Leventhal, 1979; Berner and Raiswell 1983): the ratio of normal marine sediments under non-euxinic conditions is 0.36, whereas those of euxinic and anoxic marine sediments (e.g., the Black Sea) exceed 0.36 (Berner and Raiswell 1984; Raiswell and Berner 1986). In completely anoxic marine environments, TS/TOC ratios tend to plot above the "normal marine line" because pyrite is formed by bacterial sulfate reduction within the water column and at the sea floor. The low TS/TOC ratios of both the MCMM and the UMM (Fig. 2) suggest a normal marine sediments under non-euxinic conditions while the high TS/TOC ratios of the LSM plot above the "normal marine line" indicate excess sulfur possibly due to euxinic depositional conditions. It is noteworthy that the relatively low TS contents of the lower MSM and the relatively consistent TS/TOC ratios with normal marine environment, indicates that the lower Yangtze basin had recovered to normal, oxic marine conditions by this level.

Global comparisons and links

In addition to our Lower Yangtze study area, the deep-water sections (e.g., Chaotian) of the Upper and Middle Yangtze also record anoxic/sulfidic waters in the early-middle Capitanian (Fig. 10) (Lai et al. 2008; Saitoh et al. 2013a; Shi et al. 2016), suggesting anoxia prevailed for at least several hundred kilometers along the northern Yangtze platform. Other contemporary basins (e.g., in North American, Europe, and Russia) have similar sedimentary characteristics to the Gufeng Formation (Kametaka et al.

2005), suggesting that OMZs were well developed during the late Guadalupian. However, in South China shallow water sections (e.g. Penglaitan) were well ventilated before the mid-Capitanian mass extinction (Wignall et al. 2009a, 2010), and oxygen-deficient waters only developed in the *J. granti* conodonts zone (Fig. 10) after the onset of extinction (Bond et al. 2010a,b). This redox change may also be responsible for the dramatic negative shift in sulfur isotopes in the upper Laibin limestone (from the upper *J. granti* zone to the lowest *C. postbitteri postbitteri* zone) of the Tieqiao section (Yan et al. 2013). In addition, sulfur isotopes data from other sections (Penglaitan, Teiqiao and EF sections) suggest that sulfidic waters developed sporadically in several shallow water sections (Zhang et al. 2015). Thus, the temporal-spatial record in South China shows that sulfidic waters expanded from relatively deep water in the early-middle Capitanian into shallower waters in the late Capitanian.

Within the Panthalassa Ocean the transition from red to grey-coloured chert has been used to infer the onset of a global anoxic episode that began in the mid-Capitanian and persisted into the Triassic (Isozaki, 1997, 2009b). However, the grey chert lacks pyrite, shows no signs of organic enrichment (TOC remains below 0.09 %) and is well biouturbated indicating that seafloor conditions are likely to have been only weakly dysoxic until the end of the Permian (when pyrite-rich strata develop) (Wignall et al. 2010). Nonetheless, the mid-Capitanian oceanic changes were sufficient to drive a change in radiolarian faunas from ones dominated by Pseudoalbaillela to populations of Follicucullus.

Relationship of redox changes with the extinction

Changing oceanic redox conditions could have played a major role in the radiolarian crisis as it did during the Permian-Triassic transition (e.g., Wignall et al. 2010; Feng and Algeo, 2014). The disappearance of radiolarian chert coincided with the increase in the TS values and TS/TOC ratios in the basal UMM (Fig. 2), suggesting a causal relationship between intensified anoxia and radiolarian crisis. A similar scenario

that enhanced anoxic condition caused the decrease of radiolarian, also occurred in the upper *Follicucullus scholasticus* zone in the Maocaojie section of the Middle Yangtze area (Shi et al., 2016). The radiolarian faunal changes in South China during the Capitanian coincided with the expansion of oceanic anoxia on the eastern margin of the Paleo-Tethys Ocean (e.g., Saitoh et al. 2014). In addition, the disappearance of radiolarian was also accompanied by intensified anoxic conditions in the Panthalassa Ocean and its periphery (e.g., west Texas of USA, Zhang et al., 2015).

It is also clear that the beginning of this enhanced marine anoxic condition during the earlier UMM was also concordant with the decline in the biological community in the *J. altudaensis* zone (Fig. 10). The enhanced euxinia during deposition of the shallower water Yinping Formation suggests redox-related stress also affected inner shelf seas. The oceanic record thus indicates a link between extinction and redox change, albeit in a more subdued fashion.

Implications for the mid-Capitanian mass extinction

Although further palaeontological studies of the late Guadalupian in the Lower Yangtze area are still needed, evidence from the Chaohu area suggests that the Capitanian mass extinction commenced in the middle Capitanian (the end of the *F. scholasticus–R. uralicus* zone) before the end of the stage. This timing is indicated by the $^{206}Pb/^{238}U$ dating age (261.6 ± 1.6 Ma) of the boundary tuff of the Gufeng and Yinping Formations. We therefore conclude that a biotic crisis could have begun in deep basinal settings during the early-middle Capitanian, and then peaked in the middle Capitanian, at the time of the well-constrained shallow-water extinction (*J. altudaensis-J. prexuanhanensis* conodonts zone) in the Upper Yangtze area (Wignall et al. 2009a; Bond et al. 2010b).

The frequent explosive felsic volcanic activity during the eruption of the ELIP resulted in the release of voluminous amounts of CO_2, SO_2 and acid volcanic ash, which could have led to climatic and

environmental changes, and then resulted in severe survival pressures on marine organisms. The great regression and marine anoxia-euxinia during the mid-Capitanian slightly postdate the onset of ELIP eruptions and accompanied the peak eruption phase. These environmental phenomena could have contributed to the deterioration of the marine environment via the loss of shallow-marine habitats due to emergence and spread of uninhabitable anoxic areas.

6. Conclusions

In this study, the mid-Capitanian mass extinction and related geological events have been evaluated using new evidence from the deep water slope/basin deposits of the Lower Yangtze region that reveals:

(1) Tuffs in the uppermost Gufeng Formation yield an age (*J. altudaensis* zone to *J. xuanhanensis* zone, ~263-261.5 Ma) that correlates with the initial eruption of the Emeishan flood basalts, suggesting that this province was their source. This is also confirmed by their mineralogical and geochemical characteristics.

(2) The turnover of radiolarians in basinal settings, decline of initially very high primary productivity and demise of shallow water organisms all indicate that considerable disturbances of the oceanic food web and related biotic crisis occurred during the mid-Capitanian. The Guadalupian biotic crisis was thus within Capitanian Stage and not at its termination.

(3) A major regression is seen in South China but it did not cause the deep water biotic crisis directly because it occurred later. However, the loss of the shallow-marine habitat area could have exacerbated the crisis for shallow water organisms.

(4) The decline of the biological community was in accordance with the appearance of marine anoxic condition in the *J. altudaensis* zone and further intensified by enhanced euxinia in the later Capitanian.

Acknowledgments

We thank Dr. Tianchen He and Dr. Yuce Wang for providing constructive suggestions. We acknowledge David Bond and one anonymous reviewer for their comments that substantially improved this work, as well as Graham Anthony Shields-Zhou for editorial handling.

Funding

This work was supported by the National Natural Science Foundation of China (Grant nos. U1663202, 41372127, 41172139 and 41690131) and the program B for Outstanding PhD candidate of Nanjing University.

References

Ali, J.R., Thompson, G.M., Song, X.Y. & Wang, Y.L. 2002. Emeishan Basalts (SW China) and the 'end-Guadalupian' crisis: magnetobiostratigraphic constraints. *Journal of the Geological Society*, 159, 21-29.

Ali, J.R., Thompson, G.M., Zhou, M.F. & Song, X.Y. 2005. Emeishan large igneous province, SW China. Lithos, 79, 475-489.

Altaner, S.P. 1990. Mineralogy, chemistry, and diagenesis of tuffs in the Sucker Creek Formation (Miocene), Eastern Oregon. *Clays and Clay Minerals*, 38, 561-572.

Andersen, T. 2002. Correction of common Pb in U–Pb analyses that do not report ^{204}Pb. *Chemical Geology*, 192, 59–79.

Anh, T.V., Pang, K.N, Chung, S.L., Lin, H.M., Hoa, T.T., Anh, T.T. & Yang, H.J. 2011. The Song Da magmatic suite revisited: A petrologic, geochemical and Sr-Nd isotopic study on picrites, flood basalts and silicic volcanic rocks. *Journal of Asian Earth Sciences*, 42, 1341-1355.

Belousova, E.A., Griffin, W.L., O'Reilly, S.Y. & Fisher, N.I. 2002. Igneous zircon: trace element composition as an indicator of source rock type. *Contributions to Mineralogy and Petrology*, 143, 602-622.

Berner, R.A. 1984. Sedimentary pyrite formation-an update. *Geochimica Et Cosmochimica Acta*, 48, 605-615.

Berner, R.A. & Raiswell, R. 1983. Burial of orginic-carbon and pyrite sulfur in sediments over Phanerozoic time-A new theory. Geochimica Et Cosmochimica Acta, 47: 855-862.

Berner, R.A. & Raiswell, R. 1984. C/S method for distinguishing fresh-water from marine sedimentary-rocks. Geology, 12: 365-368.

Bond, D.P.G., Hilton, J., Wignall, P.B., Ali, J.R., Stevens, L.G., Sun, Y. & Lai, X. 2010a. The Middle Permian (Capitanian) mass extinction on land and in the oceans. *Earth-Science Reviews*, 102, 100-116.

Bond, D.P.G. & Wignall, P.B. 2009. Latitudinal selectivity of foraminifer extinctions during the late Guadalupian crisis. *Paleobiology*, 35, 465-483.

Bond, D.P.G., Wignall, P.B., Joachimski, M.M., Sun, Y., Savov, I., Grasby, S.E., Beauchamp, B. & Blomeier, D.P.G. 2015. An abrupt extinction in the Middle Permian (Capitanian) of the Boreal Realm (Spitsbergen) and its link to anoxia and acidification. *Geological Society of America Bulletin*, 127, 1411-1421.

Bond, D.P.G., Wignall, P.B., Wang, W., Izon, G., Jiang, H.S., Lai, X.L., Sun, Y.D., Newton, R.J., Shao, L.Y., Vedrine, S. & Cope, H. 2010b. The mid-Capitanian (Middle Permian) mass extinction and carbon isotope record of South China. *Palaeogeography Palaeoclimatology Palaeoecology*, 292, 282-294.

Bureau of Geology and Mineral Resources of Anhui Province. 1989. Stratigtaphic record of Anhui Province. *Anhui Science and Technology Publishing House*. (in Chinese)

Canfield, D.E. 1994. Factors influencing organic-carbon preservation in marine-sediments. *Chemical Geology*, 114, 315-329.

Christidis, G.E. 1998. Comparative study of the mobility of major and trace elements during alteration of an andesite and a rhyolite to bentonite, in the Islands of Milos and Kimolos, Aegean, Greece. *Clays and Clay Minerals*, 46, 379-399.

Clapham, M.E., Shen, S. & Bottjer, D.J. 2009. The double mass extinction revisited: reassessing the severity, selectivity, and causes of the end-Guadalupian biotic crisis (Late Permian). *Paleobiology*, 35, 32-50.

De la Horra, R., Galan-Abellan, A.B., Lopez-Gomez, J., Sheldon, N.D., Barrenechea, J.F., Luque, F.J., Arche, A. & Benito, M.I. 2012. Paleoecological and paleoenvironmental changes during the continental Middle-Late Permian transition at the SE Iberian Ranges, Spain. *Global and Planetary Change*, 94-95, 46-61.

Enkin, R.J., Yang, Z.Y., Chen, Y. &nCourtillot, V. 1992. Paleomagnetic constraints on the geodynamic history of the major blocks of China from the Permian to the Present. *Journal of Geophysical Research-Solid Earth*, 97, 13953-13989.

Ernst, R.E. 2014. Geochemistry of LIPs, Part 10, Large Igneous Provinces. Cambridge University Press.

Eyuboglu, Y. 2015. Petrogenesis and U-Pb zircon chronology of felsic tuffs interbedded with turbidites (Eastern Pontides Orogenic Belt, NE Turkey): Implications for Mesozoic geodynamic evolution of the eastern Mediterranean region and accumulation rates of turbidite sequences. *Lithos*, 212, 74-92.

Fang Q., Hong H., Chen Z., Yu, J., Wang, C., Yin, K., Zhao, L., Liu, Z., Cheng, F., Gong, N. & Fumes., H. 2017. Microbial proliferation coinciding with volcanism during the Permian–Triassic transition: New, direct evidence from volcanic ashes, South China. *Palaeogeography Palaeoclimatology Palaeoecology*, 474, 164-186.

Feng, Q. & Algeo, T. J. 2014. Evolution of oceanic redox conditions during the Permo-Triassic transition: evidence from deepwater radiolarian facies. *Earth-Science Reviews,* 137, 34-51.

Frost, C.D. & Frost, B.R. 2011. On Ferroan (A-type) Granitoids: their Compositional Variability and Modes of Origin. *Journal of Petrology*, 52, 39-53.

Gand, G. & Durand, M. 2006. Tetrapod footprint ichno-associations from French Permian basins. Comparisons with other Euramerican ichnofaunas. *Geological Society London Special Publications*, 265, 157-177.

Gradstein, F.M., Ogg, J.G. & Hilgen, F.J. 2012. On the Geologic time scale. *Newslett. Stratigr*. 45, 171–188.

Griffin, W.L., Belousova, E.A., Shee, S.R., Pearson, N.J. & O'Reilly, S.Y. 2004. Archean crustal evolution in the northern Yilgam Craton: U-Pb and Hf-isotope evidence from detrital zircons. *Precambrian Research*, 131, 231-282.

Groves, J.R. & Wang, Y. 2013. Timing and size selectivity of the Guadalupian (Middle Permian) fusulinoidean extinction. *Journal of Paleontology*, 87, 183-196.

Hallam, A. & Wignall, P.B. 1999. Mass extinctions and sea-level changes. *Earth-Science Reviews*, 48, 217-250.

Haq, B.U. & Schutter, S.R. 2008. A chronology of Paleozoic sea-level changes. *Science*, 322, 64-68.

Harris, N.B.W., Pearce, J.A. & Tindle, A.G. 1986. Geochemical characteristics of collision-zone magmatism. In: Coward, M.P., Ries, A.C. (Eds.), Collision Tectonics, Geological Society, London, Special Publication.

Hastie, A.R., Kerr, A.C., Pearce, J.A. & Mitchell, S.F. 2007. Classification of altered volcanic island arc rocks using immobile trace elements: Development of the Th-Co discrimination diagram. *Journal of Petrology*, 48, 2341-2357.

Hayashi, K., Fujisawa, H., Holland, H.D. & Ohmoto, H. 1997. Geochemistry of similar to 1.9 Ga sedimentary rocks from northeastern Labrador, Canada. *Geochimica Et Cosmochimica Acta*, 61, 4115-4137.

He, B., Xu, Y., Chung., S., Xiao, L. & Wang, Y. 2003. Sedimentary evidence for a rapid, kilometer-scale crustal doming prior to the eruption of the Emeishan flood basalts.*Earth & Planetary Science Letters*, 213, 391-405.

He, B., Xu, Y. & Campbell, I. 2009. Pre-eruptive uplift in the Emeishan? *Nature Geoscience*, 2, 530-531.

He, B., Xu, Y., Huang, X., Luo, Z., Shi, Y., Yang, Q. & Yu, S. 2007. Age and duration of the Emeishan flood volcanism, SW China: Geochemistry and SHRIMP zircon U-Pb dating of silicic ignimbrites, post-volcanic Xuanwei Formation and clay tuff at the Chaotian section. *Earth and Planetary Science Letters*, 255, 306-323.

He, B., Xu, Y., Zhong, Y. & Guan, J. 2010. The Guadalupian-Lopingian boundary mudstones at Chaotian (SW China) are clastic rocks rather than acidic tuffs: Implication for a temporal coincidence between the end-Guadalupian mass extinction and the Emeishan volcanism. *Lithos*, 119, 10-19.

He, B., Zhong, Y., Xu, Y. & Li, X. 2014. Triggers of Permo-Triassic boundary mass extinction in South China: the Siberian Traps or Paleo-Tethys ignimbrite flare-up? *Lithos*, 204, 258-267.

He, W., Wu, S., Zhang, K. & Bu, J. 1999. Classification of Radiolarian fossil zones and environmental analysis of Gufeng Formation in Lower Yangtze Region. *Journal of Jiangsu Geology*, 23: 17-23. (in Chinese, with English Abstr.)

Hu, S.Z. 1983. The division and correlations of Lungtan Formation in south Jiangsu province and the discussion on the regulation of sea transgression and regression. *Journal of Changchun University of Geosciences*, 4, 49-59. (in Chinese)

Huang, H., Du, Y., Yang, J., Zhou, L., Hu, L., Huang, H. & Huang, Z. 2014. Origin of Permian basalts and clastic rocks in Napo, Southwest China: Implications for the erosion and eruption of the Emeishan large igneous province. *Lithos*, 208, 324-338.

Huang, Y., Chen, Z-Q., Wignall, P., Grasby, S., Zhao, L., Wang, X. & Kaiho K. 2019 Biotic responses to volatile volcanism and environmental stresses over the Guadalupian-Lopingian (Permian) transition. *Geology,* in press, doi: https://doi.org/10.1130/G45283.1

Isozaki, Y. 1997. Permo-triassic boundary superanoxia and stratified superocean: Records from lost deep sea. *Science*, 276, 235-238.

Isozaki, Y. 2009a. Illawarra Reversal: The fingerprint of a superplume that triggered Pangean breakup and the end-Guadalupian (Permian) mass extinction. *Gondwana Research*, 15, 421-432.

Isozaki, Y. 2009b. Integrated "plume winter" scenario for the double-phased extinction during the Paleozoic-Mesozoic transition: The G-LB and P-TB events from a Panthalassan perspective. *Journal of Asian Earth Sciences*, 36(6), 459-480.

Isozaki, Y., Aljinovic, D. & Kawahata, H. 2011. The Guadalupian (Permian) Kamura event in European Tethys. *Palaeogeography Palaeoclimatology Palaeoecology*, 308, 12-21.

Isozaki, Y., Kawahata, H. & Ota, A. 2007. A unique carbon isotope record across the Guadalupian-Lopingian (Middle-Upper Permian) boundary in mid-oceanic paleo-atoll carbonates: The high-productivity "Kamura event" and its collapse in Panthalassa. *Global and Planetary Change*, 55, 21-38.

Isozaki, Y. & Servais, T. 2018. The Hirnantian (Late Ordovician) and end-Guadalupian (Middle Permian) mass-extinction events compared. Lethaia, 51, 173–186. https://doi.org/10.1111/let.12252

Ito, T., Feng, Q. & Matsuoka, A. 2013. Radiolarian faunal change in the Middle Permian Gufeng Formation in the Liuhuang section, Chaohu, South China. *Science Reports of Niigata University (Geology)*, 28, 39-49.

Ito, T., Feng, Q. L. & Matsuoka, A. 2016. Possible boundaries between Pseudoalbaillella and Follicucullus (Follicucullidae, Albaillellaria, Radiolaria): An example of morphological information from fossils and its use in taxonomy. *Forma*, 31, 7-10.

Jackson, S.E., Pearson, N.J., Griffin, W.L. & Belousova, E.A. 2004. The application of laser ablation-inductively coupled plasma-mass spectrometry to in situ U-Pb zircon geochronology. *Chemical Geology*, 211, 47-69.

Jin, Y.G. & Hu, S.Z. 1978. Brachiopod fossils of the Kuhfeng Formation in South Anhui Province and Ningzhen Mountains. *Acta Palaeontologica Sinica*, 17, 101-128. (in Chinese)

Jin, Y., Shen, S., Henderson, C.M., Wang, X., Wang, W., Wang, Y., Cao, C. & Shang, Q. 2006. The Global Stratotype Section and Point (GSSP) for the boundary between the Capitanian and Wuchiapingian stage (Permian). *Episodes*, 29, 253-262.

Kaiho, K., Chen, Z.Q., Ohashi, T., Arinobu, T., Sawada, K. & Cramer, B.S. 2005. A negative carbon isotope anomaly associated with the earliest Lopingian (Late Permian) mass extinction. *Palaeogeography Palaeoclimatology Palaeoecology*, 223, 172-180.

Kametaka, M., Nagai, H., Zhu, S. & Takebe, M. 2009. Middle Permian radiolarians from Anmenkou, Chaohu, Northeastern Yangtze platform, China. *Island Arc*, 18, 108-125.

Kametaka, M., Takebe, M., Nagai, H., Zhu, S. & Takayanagi, Y. 2005. Sedimentary environments of the Middle Permian phosphorite-chert complex from the northeastern Yangtze platform, China; the Gufeng Formation: a continental shelf radiolarian chert. *Sedimentary Geology*, 174, 197-222.

Kani, T., Hisanabe, C. & Isozaki, Y. 2013. The Capitanian (Permian) minimum of Sr^{87}/Sr^{86} ratio in the mid-Panthalassan paleo-atoll carbonates and its demise by the deglaciation and continental doming. *Gondwana Research*, 24, 212-221.

Kuwahara, K., Yao, A., Yao, J. X. & Wang, X. 2007. Permian radiolarians from the Gufeng Formation of the Tongling area, Anhui Province, China. *Jour. Geosciences, Osaka City Univ.*, 50, 35–54.

Lai, X., Wang, W., Wignall, P.B., Bond, D.P.G., Jiang, H., Ali, J.R., John, E.H. & Sun, Y. 2008. Palaeoenvironmental change during the end-Guadalupian (Permian) mass extinction in Sichuan, China. *Palaeogeography Palaeoclimatology Palaeoecology*, 269, 78-93.

Leven, E.Y. 2003. Diversity dynamics of fusulinid genera and main stages of their evolution. *Stratigraphy and Geological Correlation*, 11, 220-230.

Leventhal, J.S. 1979. The relationship between organic carbon and sulfide sulfur in re- cent and ancient marine and euxinic sediments. *Eos, Trans. Amer. Geophys. Union*, 60, 286.

Li, X., Li, Z., Li, W. & Wang, Y. 2006. Initiation of the Indosinian Orogeny in South China: evidence for a Permian magmatic arc on Hainan Island. *Journal of Geology*, 114, 341–353.

Liao, Z., Hu, W., Cao, J., Wang, X., Yao, S., Wu, H. & Wan, Y. 2016. Heterogeneous volcanism across the Permian–Triassic Boundary in South China and implications for the Latest Permian Mass Extinction: New evidence from volcanic ash layers in the Lower Yangtze Region. *Journal of Asian Earth Sciences*, 127, 197-210.

Lucas, S.G. 2009. Timing and magnitude of tetrapod extinctions across the Permo-Triassic boundary. *Journal of Asian Earth Sciences*, 36, 491-502.

Ludwig, K.R. 2012. Isoplot 3.75, A geochronological Toolkit for Excel. 5. Berkeley Geochronology Center Special, Publication.

Ma, Q. & Feng, Q. 2012. Taxonomy and biostratigraphy of the Middle Permian radiolarian fauna from the Gufeng Formation in Luojiaba, West Hubei Province. *Acta Micropalaeontologica Sinica*, 29, 402-415. (in Chinese, with English Abstr.)

Ma, Q., Feng, Q., Caridroit, M., Danelian, T. & Zhang, N. 2016. Integrated radiolarian and conodont biostratigraphy of the Middle Permian Gufeng Formation (South China). *Comptes Rendus Palevol*, 15, 453-459.

McLennan, S.M., Nance, W.B. & Taylor, S.R. 1980. Rare-earth element-thorium correlations in sedimentary-rocks, and the composition of the continental crust. *Geochimica Et Cosmochimica Acta*, 44, 1833-1839.

Mei, S. 1998. Conodont succession of the Guadalupian-Lopingian boundary strata in Laibin of Guangxi, China and West Texas, USA. *Palaeoworld*, 9, 53-76.

Morse, J.W. & Emeis, K.C. 1990. Controls on C/S ratios in hemipelagic upwelling sediments. *American Journal of Science*, 290, 1117-1135.

Nestell, G.P. & Nestell, M.K. 2010. Late Capitanian (latest Guadalupian, Middle Permian) radiolarians from the Apache Mountains, West Texas. *Micropaleontology*, 56, 7–68.

Nielsen, J.K. & Shen, Y. 2004. Evidence for sulfidic deep water during the Late Permian in the East Greenland Basin. *Geology*, 32, 1037-1040.

Nishikane, Y., Kaiho, K., Henderson, C.M., Takahashi, S. & Suzuki, N. 2014. Guadalupian-Lopingian conodont and carbon isotope stratigraphies of a deep chert sequence in Japan. *Palaeogeography Palaeoclimatology Palaeoecology*, 403, 16-29.

Ota, A. & Isozaki, Y. 2006. Fusuline biotic turnover across the Guadalupian-Lopingian (Middle-Upper Permian) boundary in mid-oceanic carbonate buildups: Biostratigraphy of accreted limestone in Japan. *Journal of Asian Earth Sciences*, 26, 353-368.

Raiswell, R. & Berner, R.A. 1986. Pyrite and organic-matter in Phanerozoic normal marine shales. *Geochimica Et Cosmochimica Acta*, 50, 1967-1976.

Ramezani, J. & Bowring, S.A. 2017. Advances in numerical calibration of the Permian timescale based on radioisotopic geochronology. *Geological Society, London, Special Publications*, 450, 450-17.

Retallack, G.J., Metzger, C.A., Greaver, T., Jahren, A.H., Smith, R.M.H. & Sheldon, N.D. 2006. Middle-Late Permian mass extinction on land. *Geological Society of America Bulletin*, 118, 1398-1411.

Rickwood, P.C. 1989. Boundary lines with petrologic diagrams which use oxides of major and minor elements. *Lithos*, 22, 247-263.

Rollinson, H.R. 1993. Using trace element data, part 4. Using Geochemical Data Book: Evaluation, Presentation, Interpretation. John Wiley & Sons Inc., New York.

Ross, C.A. & Ross, J.R.P. 1985. Late Paleozoic depositional sequences are synchronous and worldwide. *Geology*, 13, 194-197.

Rubatto, D. 2002. Zircon trace element geochemistry: partitioning with garnet and the link between U-Pb ages and metamorphism. *Chemical Geology*, 184, 123-138.

Saitoh, M., Isozaki, Y., Ueno, Y., Yoshida, N., Yao, J. & Ji, Z. 2013. Middle-Upper Permian carbon isotope stratigraphy at Chaotian, South China: Pre-extinction multiple upwelling of oxygen-depleted water onto continental shelf. *Journal of Asian Earth Sciences*, 67-68, 51-62.

Saitoh, M., Isozaki, Y., Yao, J., Ji, Z., Ueno, Y. & Yoshida, N. 2013. The appearance of an oxygen-depleted condition on the Capitanian disphotic slope/basin in South China: Middle-Upper Permian stratigraphy at Chaotian in northern Sichuan. *Global and Planetary Change*, 105, 180-192.

Saitoh, M., Ueno, Y., Isozaki, Y., Nishizawa, M., Shozugawa, K., Kawamura, T., Yao, J., Ji, Z., Takai, K., Yoshida, N. & Matsuo, M. 2014. Isotopic evidence for water-column denitrification and sulfate reduction at the end-Guadalupian (Middle Permian). *Global and Planetary Change*, 123, 110-120.

Shellnutt, J.G. & Jahn, B.M. 2010. Formation of the Late Permian Panzhihua plutonic-hypabyssal-volcanic igneous complex: Implications for the genesis of Fe-Ti oxide deposits and A-type granites of SW China. *Earth and Planetary Science Letters*, 289, 509-519.

Shellnutt, J.G. & Zhou, M.F. 2007. Permian peralkaline, peraluminous and metaluminous A-type granites in the Panxi district, SW China: Their relationship to the Emeishan mantle plume. *Chemical Geology*, 243, 286-316.

Shen, S. & Shi, G. 2002. Paleobiogeographical extinction patterns of Permian brachiopods in the Asian–western Pacific region. *Paleobiology*, 28, 449-463.

Shen, S. & Shi, G. 2009. Latest Guadalupian brachiopods from the Guadalupian/Lopingian boundary GSSP section at Penglaitan in Laibin, Guangxi, South China and implications for the timing of the pre-Lopingian crisis. *Palaeoworld*, 18, 152-161.

Shen, S., Wang, Y., Henderson, C.M., Cao, C. & Wang, W. 2007. Biostratigraphy and lithofacies of the Permian System in the Laibin-Heshan area of Guangxi, South China. *Palaeoworld*, 16, 120-139.

Shi, L., Feng, Q., Shen, J., Ito, T. & Chen, Z. 2016. Proliferation of shallow-water radiolarians coinciding with enhanced oceanic productivity in reducing conditions during the Middle Permian, South China: evidence from the Gufeng Formation of western Hubei Province. *Palaeogeography Palaeoclimatology Palaeoecology*, 444, 1-14.

Smolarek, J., Marynowski, L., Trela, W., Kujawski, P. & Simoneit, B.R.T. 2017. Redox conditions and marine microbial community changes during the end-Ordovician mass extinction event. *Global and Planetary Change*, 149, 105-122.

Spears, D.A. 2012. The origin of tonsteins, an overview, and links with seatearths, fireclays and fragmental clay rocks. *International Journal of Coal Geology*, 94, 22-31.

Spears, D.A. & Kanaris-sotiriou, R. 1979. Geochemical and mineralogical investigation of some British and other European tonsteins. *Sedimentology*, 26, 407-425.

Stanley, S.M. & Yang, X. 1994. A double mass extinction at the end of the Paleozoic era. *Science*, 266, 1340-1344.

Stanley, S. M. 2016. Estimates of the magnitudes of major marine mass extinctions in earth history. Proceedings of the National Academy of Sciences, 113, E6325–E6334. https://doi.org/10.1073/pnas.1613094113

Sun, D. & Xia, W. 2006. Identification of the Guadalupian-Lopingian boundary in the Permian in a bedded chert sequence, south china. *Palaeogeography Palaeoclimatology Palaeoecology*, 236(3), 272-289.

Sun, S. & McDonough, Q.F. 1989. Chemical and isotopic systematic of oceanic basalts; implications for mantle compositions and processes. In: Saunders, A.D., Norry.

Sun, Y., Lai, X., Wignall, P.B., Widdowson, M., Ali, J.R., Jiang, H., Wang, W., Yan, C., Bond, D.P.G. & Vedrine, S. 2010. Dating the onset and nature of the Middle Permian Emeishan large igneous province eruptions in SW China using conodont biostratigraphy and its bearing on mantle plume uplift models. *Lithos*, 119, 20-33.

Taylor, S.R. & Mclennan, S.M. 1985. The Continental Crust: Its Composition and Evolution. Blackwell, Oxford, UK.

Wang, W., Cao, C. & Wang, Y. 2004. The carbon isotope excursion on GSSP candidate section of Lopingian-Guadalupian boundary. *Earth and Planetary Science Letters*, 220, 57-67.

Wang, J. & Jin, Y. 2000. Permian palaeogeographic evolution of the Jiangnan Basin, South China. *Palaeogeography Palaeoclimatology Palaeoecology*, 160, 35-44.

Wang, X.D. & Sugiyama, T. 2000. Diversity and extinction patterns of Permian coral faunas of China. *Lethaia*, 33, 285-294.

Wang, Y. & Qi, D. 1995. Radiolarian fauna of the Kuhfeng Formation in Southern part of Jiangsu and Anhui provinces. *Acta Micropalaeontologica Sinica*, 12: 374-387.

Wang, Y., & Yang, Q. 2011. Biostratigraphy, phylogeny and paleobiogeography of Carboniferous–Permian radiolarians in South China. *Palaeoworld*, 20, 134-145.

Wignall, P.B. 2015. The Worst of Times: How life on Earth survived eighty million years of extinctions. Princeton University Press, Princeton.

Wignall, P.B., Bond, D.P.G., Haas, J., Wang, W., Jiang, H., Lai, X., Altiner, D., Vedrine, S., Hips, K., Zajzon, N., Sun, Y. & Newton, R.J. 2012. Capitanian (Middle Permian) mass extinction and recovery in western Tethys: a fossil, facies, and delta C^{13} study from Hungary and Hydra Island (Greece). *Palaios*, 27, 78-89.

Wignall, P.B., Bond, D.P.G., Kuwahara, K., Kakuwa, Y., Newton, R.J. & Poulton, S.W. 2010. An 80 million year oceanic redox history from Permian to Jurassic pelagic sediments of the Mino-Tamba terrane, SW Japan, and the origin of four mass extinctions. *Global and Planetary Change*, 71, 109-123.

Wignall, P.B., Sun, Y., Bond, D.P.G., Izon, G., Newton, R.J., Vedrine, S., Widdowson, M., Ali, J.R., Lai, X., Jiang, H., Cope, H. & Bottrell, S.H. 2009a. Volcanism, mass extinction, and carbon isotope fluctuations in the Middle Permian of China. *Science*, 324, 1179-1182.

Wignall, P.B., Vedrine, S., Bond, D.P.G., Wang, W., Lai, X.L., Ali, J.R. & Jiang, H.S. 2009b. Facies analysis and sea-level change at the Guadalupian-Lopingian Global Stratotype (Laibin, South China), and its bearing on the end-Guadalupian mass extinction. *Journal of the Geological Society*, 166, 655-666.

Winchester, J.A. & Floyd, P.A. 1977. Geochemical discrimination of different magma series and their differentiation products using immobile elements. *Chemical Geology*, 20, 325-343.

Wu, K., Ma, Q. & Feng, Q. 2015. Stratigraphic division and spatial distribution of the Middle Permian Kuhfeng Formation in the northern Yangtze block. *Journal of Stratigraphy*, 39, 33-39. (in Chinese, with English Abstr.)

Wu, Q., Ramezani, J., Zhang, H., Wang, T.T., Yuan, D.X., Mu, L., Zhang, Y.C., Li, X.H. & Shen, S.Z. 2017. Calibrating the Guadalupian Series (Middle Permian) of South China. *Palaeogeography, Palaeoclimatology, Palaeoecology*, 466, 361-372.

Wu, Y. & Zheng, Y. 2004. Genesis of zircon and its constraints on interpretation of U-Pb age. *Chinese Science Bulletin*, 49, 1554-1569. (in Chinese, with English Abstr.)

Xiao, Y., Suzuki, N. & He, W. 2018. Low-latitudinal standard Permian radiolarian biostratigraphy for multiple purposes with Unitary Association, Graphic Correlation, and Bayesian inference methods. *Earth-Science Reviews*, 179, 168-206.

Xu, Y., Chung, S., Jahn, B. & Wu, G. 2001. Petrologic and geochemical constraints on the petrogenesis of Permian-Triassic Emeishan flood basalts in southwestern China. *Lithos*, 58, 145-168.

Xu, Y., Chung, S., Shao, H. & He, B. 2010. Silicic magmas from the Emeishan large igneous province, Southwest China: Petrogenesis and their link with the end-Guadalupian biological crisis. *Lithos*, 119, 47-60.

Xu, Y., Luo, Z., Huang, X., He, B., Xiao, L., Xie, L. & Shi, Y. 2008. Zircon U-Pb and Hf isotope constraints on crustal melting associated with the Emeishan mantle plume. *Geochimica Et Cosmochimica Acta*, 72, 3084-3104.

Xue, W., Li, B., Yan, J., Ellwood, B.B., Tomkin, J.H., Wang, Y. & Zhu, Z. 2015. High-resolution floating point time scale (FPTS) of Permian Capitanian Stage in South China. *Chinese Journal of Geophysics-Chinese Edition*, 58, 3719-3734. (in Chinese, with English Abstr.)

Yan, D., Zhang, L. & Qiu, Z. 2013. Carbon and sulfur isotopic fluctuations associated with the end-Guadalupian mass extinction in South China. *Gondwana Research*, 24, 1276-1282.

Yang, J., Cawood, P.A. & Du, Y. 2015. Voluminous silicic eruptions during late Permian Emeishan igneous province and link to climate cooling. *Earth and Planetary Science Letters*, 432, 166-175.

Yang, X., Liu, J. & Shi, G. 2004. Extinction process and patterns of Middle Permian Fusulinaceans in southwest China. *Lethaia*, 37, 139-147.

Yao, X., Zhou, Y. & Hinnov, L.A. 2015. Astronomical forcing of a Middle Permian chert sequence in Chaohu, South China. *Earth and Planetary Science Letters*, 422, 206-221.

Yuan, D. X., Shen, S. Z. & Henderson, C. M. 2017. Revised Wuchiapingian conodont taxonomy and succession of South China. Journal of Paleontology, 91, 1199–1219. https://doi.org/10.1017/jpa.2017.71

Zhang, B., Yao, S., Wignall, P., Hu, W., Ding, H., Liu, B. & Ren, Y. 2018. Widespread coastal upwelling along the Eastern Paleo-Tethys Margin (South China) during the Middle Permian (Guadalupian): Implications for organic matter accumulation. Marine and Petroleum Geology, 97, 113-126.

Zhang, C., Zhang, C., She, Z. & Yin, K. 2005. Volcanic Ash in the Clay Rocks from Upper Shaximiao Formation of Middle Jurassic, Northeast of Sichuan Basin: Evidence from Petrology, Mineralogy and Geochemistry. *Geological journal of China universities*, 11, 415-424. (in Chinese, with English Abstr.)

Zhang, G., Zhang, X., Li, D., Farquhar, J., Shen, S., Chen, X. & Shen, Y. 2015. Widespread shoaling of sulfidic waters linked to the end-Guadalupian (Permian) mass extinction. *Geology*, 43, 1091-1094.

Zhang, S., Zhao, L. & Tong, J. 2007. Study on the claystone near the Permian-Triassic boundary from the Daxiakou section, Xingshan, Hubei Province. *Journal of Mineralogy & Petrology*, 27, 94-100. (in Chinese, with English Abstr.)

Zhang, Y., Luo, Y. & Yang, Z. 1988. Panxi Rift. Geological Publishing House, Beijing. (in Chinese)

Zhao, Y., Xu, J. & Huang, G. 1983. The division and correlation of the Late Maokou-aged strata in central Anhui-the establishment of the Yinping Formation and its significance. *Regional Geology of China*, 5, 65-76. (in Chinese, with English Abstr.)

Zheng, L., Yang, Z., Tong, Y. & Yuan, W. 2010. Magnetostratigraphic constraints on two-stage eruptions of the Emeishan continental flood basalts. *Geochemistry Geophysics Geosystems*, 11.

Zhong, Y., He, B., Mundil, R. & Xu, Y. 2014. CA-TIMS zircon U-Pb dating of felsic ignimbrite from the Binchuan section: Implications for the termination age of Emeishan large igneous province. *Lithos*, 204, 14-19.

Zhong, Y., He, B. & Xu, Y. 2013. Mineralogy and geochemistry of claystones from the Guadalupian-Lopingian boundary at Penglaitan, South China: Insights into the pre-Lopingian geological events. *Journal of Asian Earth Sciences*, 62, 438-462.

Zhou, L. & Kyte, F.T. 1988. The Permian-Triassic boundary event-a geochemical study of 3 Chinese sections. *Earth and Planetary Science Letters*, 90, 411-421.

Zhou, M., Malpas, J., Song, X., Robinson, P.T., Sun, M., Kennedy, A.K., Lesher, C.M. & Keays, R.R. 2002. A temporal link between the Emeishan large igneous province (SW China) and the end-Guadalupian mass extinction. *Earth and Planetary Science Letters*, 196, 113-122.

Zhou M., Luo, T., Huang, Z., Long, H. & Yang, Y. 2007. Advances in research on K-bentonite. *Acta Mineralogica Sinica*, 27, 351-359. (in Chinese, with English Abstr.)

Zhou, Y., Ren, Y. & Bohor, B.F. 1982. Origin and distribution of tonsteins in Late Permian coal seams of Southwestern China. *International Journal of Coal Geology*, 2, 49-77.

Zhu, Z.Y., Jiang, S.Y., Liu, G.X. & Zhao, K.D. 2013. Precise dating of the Middle Permian: Zircon U–Pb geochronology from volcanic ash beds in the basal Gufeng Formation, Yangtze region, South China. *Gondwana Research*, 23, 1599-1606.

Ziegler, A.M., Hulver, M.L. & Rowley, D.B. 1997. Permian world topography and climate. In: Martini, I.P. (Ed.), Late Glacial and Postglacial Environmental Changes-Quaternary, Carboniferous–Permian, and Proterozoic. Oxford Univ. Press, New York.

Figure captions

Fig. 1 Palaeogeography, geological setting and geographic location of the study area. (a) Paleogeographic map of the Late Guadalupian (based on Ziegler et al 1997 with modifications of Ali et al. (2005), Isozaki (2009a), Isozaki et al. (2011), Kani et al. (2013), and Saitoh et al. (2013) showing the relative position of the ELIP, Chaotian section, Chaohu section, Penglaitan and Tieqiao Section, Deep ocean Chert Section, Atoll Carbonate Section. (b) Late Guadalupian paleogeographic reconstructions of South China (modified from Sun et al. 2010; Yao et al. 2015). (c) Location of Chaohu region in the Lower Yangtze area, South China. (d) Geological setting of Chaohu region. Anmenkou Section is the research site of Kametaka et al. (2005, 2009).

Fig. 2 Lithostratigraphy, biostratigraphy and chemostratigraphy of the Gufeng and lower Yinping Formation in Chaohu region. The Gufeng Formation is divided into the Lower Phosphate Nodule bearing Mudstone Member (LPMM), Middle Chert-Mudstone Member (MCMM) and Upper Mudstone Member (UMM). The Lower Yingping Formation includes the Lower Shale Member (LSM) and lower part of the Middle Shale Member (MSM). The composite geological time is based on Kametaka et al. 2005, 2009; Gradstein et al. 2012; Zhu et al. 2013; Yao et al. 2015; Ma et al. 2016; Wu et al. 2017; Ramezani and Bowring 2017. The biostratigraphy and the relative abundance of radiolarian assemblage is from Wang and Qi (1995), He et al. (1999), Kametaka et al.(2009), Wang and Qun (2011) and Ito et al. (2013). The red dashed line show the average value for normal marine TS/TOC values (Berner and Raiswell 1984). Abbreviations: Ser. = Series, Stg. = Stage, Form. = Formation, Bioz. = Biozone, Dep. = Depth, Litho. = Lithology, Sam. = Sample.

Fig. 3 Field photographs of the Pingdingshan section. (a) Overview of the Gufeng Formation. Disconformity showing an irregular surface between limestone of the Qixia Formation (P1q) and mudstone of the Gufeng Formation (P2g). (b) A close view of conformity 23 between mudstone of the Gufeng Formation and shale of the Yingping Formation. Numbers 1 to 6 indicate the locations of the photographs shown in panels (c) to (h), respectively. (c-e, i) A close view of volcanic ash, black chert and siliceous mudstone of the upper MCMM. (f) Carbonaceous mudstone of the UMM. (h) Parallel bedding of grey shale of the LSM. (g, j) Volcanic ash (CH-3, PDS-5) of the top UMM. (k) A close view of disconformity between mudstone of the Yinping Formation (P2y) and sandstone of the Longtan Formation (P3l). The hammer is ~30cm long in b, f and k.

Fig. 4 Photomicrographs showing the lithological characteristics of the Pingdingshan strata. (a) Black chert containing abundant spheroidal radiolarians (Sample CH-24 are from the MCMM). (b) Brown siliceous mudstone containing little spheroidal radiolarians (Sample CH-40 are from the MCMM). (c) Tuff composed of quartz, feldspar, zircon and sericite grains in a clay mineral-rich matrix. (d) Zircon grain is clear, pale and euhedral crystals with well-developed tetragonal dipyramids. (e) Corroded and embayed quartz (red arrows) and euhedral hexagonal bipyramid quartz (blue arrows). (f) Laminated grey shales with a few fossils (Sample CH-72 are from the LSM). (g-h) Grey shale with abundant bivalves and ostracoda (Sample CH-64 are from the LSM). (i) Beds of small bivalves in the grey shale (Sample CH-66 are from the LSM).

Fig. 5 Cathodoluminescence images and LA-ICP-MS zircon U-Pb Concordia diagrams of zircons from sample CH-3 and PDS-5 in the Pingdingshan section, showing the analyzed spots and weighted mean 206Pb/23841 U ages.

Fig. 6 Representative XRD patterns of tuff samples from the Pingdingshan section. Abbreviations: I=illite, I/S = mixed layer illite-smectite, K = kaolinite, Qz = quartz, Mus=muscovite, Zr=zircon, Py=pyrite.

Fig. 7 Primitive mantle-normalized trace elements spider diagram 45 of tuffs from the Gufeng Formation

of the Pingdingshan section. Normalized values for primitive mantle are from Sun and McDonough (1989).

Fig. 8 Chondrite normalized REE patterns of tuffs from Gufeng Formation of the Pingdingshan section. Normalization values are from Sun and McDonough (1989). The field of ELIP felsic silicic rocks are after Anh et al. (2011), Shellnutt and Jahn (2010) and Xu et al. (2010). The field of GLB mudstones and tuffs are from He et al. (2007, 2010) and Zhong et al. (2013).

Fig. 9 Crossplot of TOC versus TS for samples from the upper Gufeng Formation and the lower middle Yingping Formation. The green line indicate the TS/TOC values of normal marine (Berner and Raiswell 1984).

Fig. 10 Correlation chart for sections with robust conodont age, zircon U-Pb age and high resolution floating point time scale control all over the world (modified from Sun et al. 2010; data of deep sea chert section are from Wignall et al. 2010; data of atoll carbonate are from Isozaki et al. 2007; data of West Texas are from Zhang et al. 2015). The figure is not to scale.

Fig. 11 (a) Bivariate plots of TiO_2 (wt.%) and Al_2O_3 (wt.%) of tuffs (modified from Hayashi et al. 1997; He et al. 2010). Mafic and felsic area of the ELIP from Zhang et al. (1988) and Xu et al. (2001). (b) TiO_2/Zr versus Nb/Y diagram of tuffs (after Winchester and Floyd (1977)). The field of ELIP felsic silicic rocks are after He et al. (2007, 2010), Shellnutt and Jahn (2010), Xu et al. (2010), Anh et al. (2011) and Zhong et al. (2013). The field of ELIP basalts is after Huang et al. (2014). (c) Th-Co classification diagrams for the felsic tuffs (after Hastie et al. 2007). (d) K_2O-SiO_2 classification diagrams for the felsic tuffs (after Rickwood 1989).

Fig. 12 (a) Hf-(Rb/10)-(Ta x 3) and (b) Hf-(Rb/30)-(Ta x 3) tectonic discrimination diagrams of the volcanic rocks (after Harris et al. 1986) showing the field of ELIP felsic rocks (He et al. 2007, 2010; Shellnutt and Jahn 2010; Xu et al. 2010; Anh et al. 2011; Zhong et al. 2013).

Fig. 1

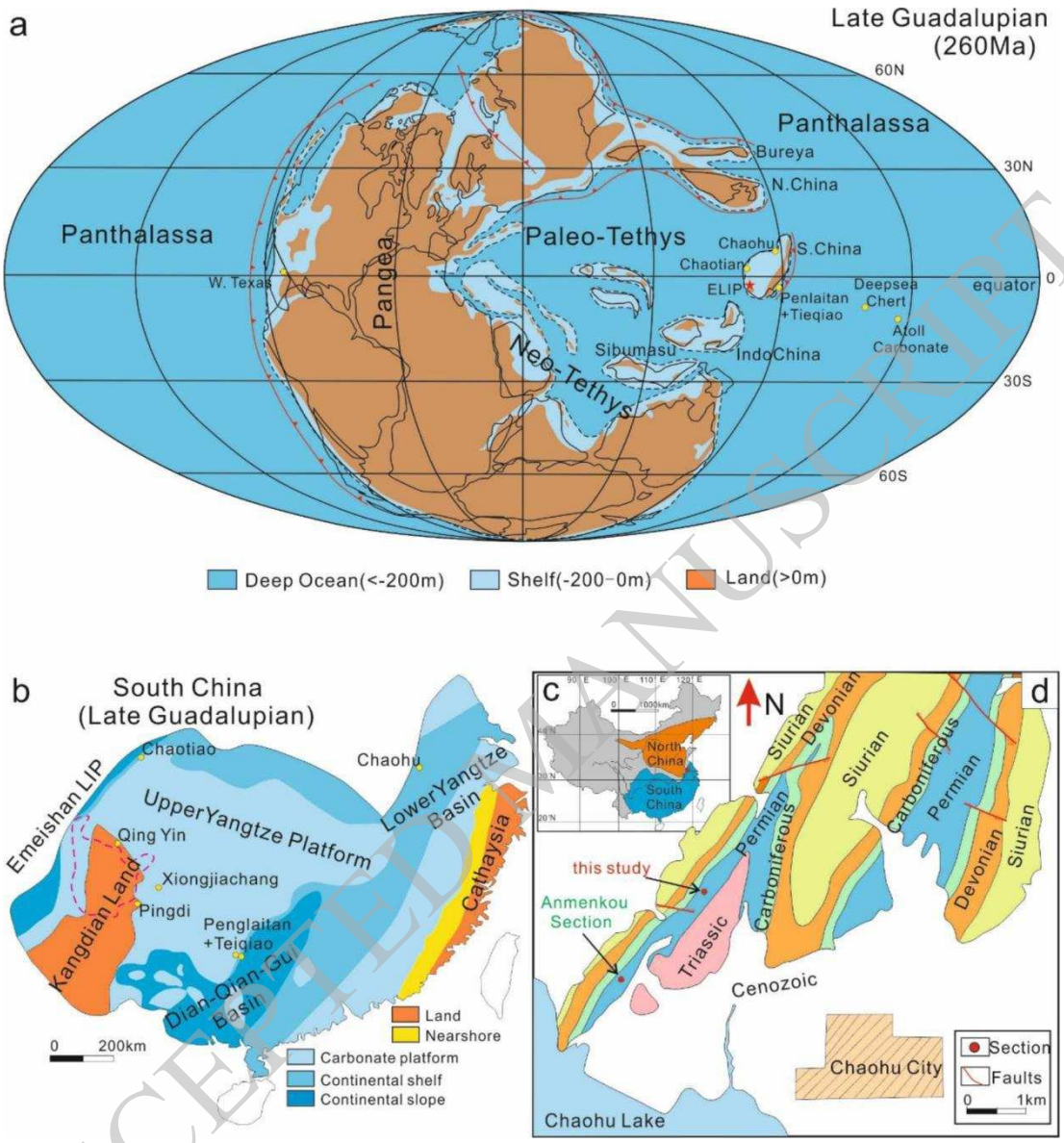

Fig. 2

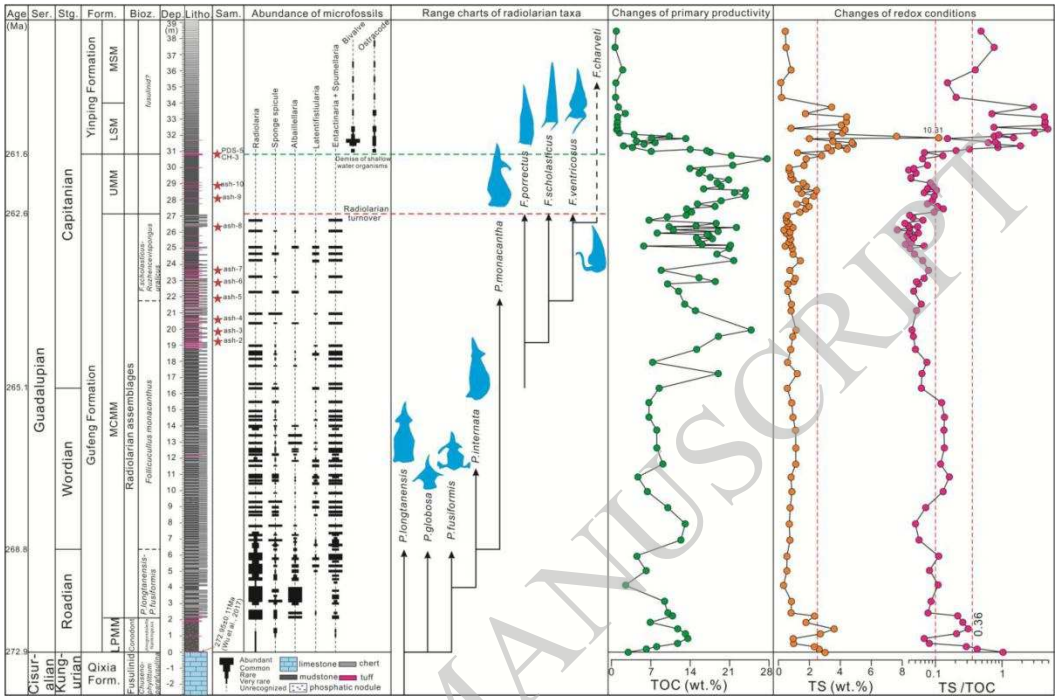

Fig. 3

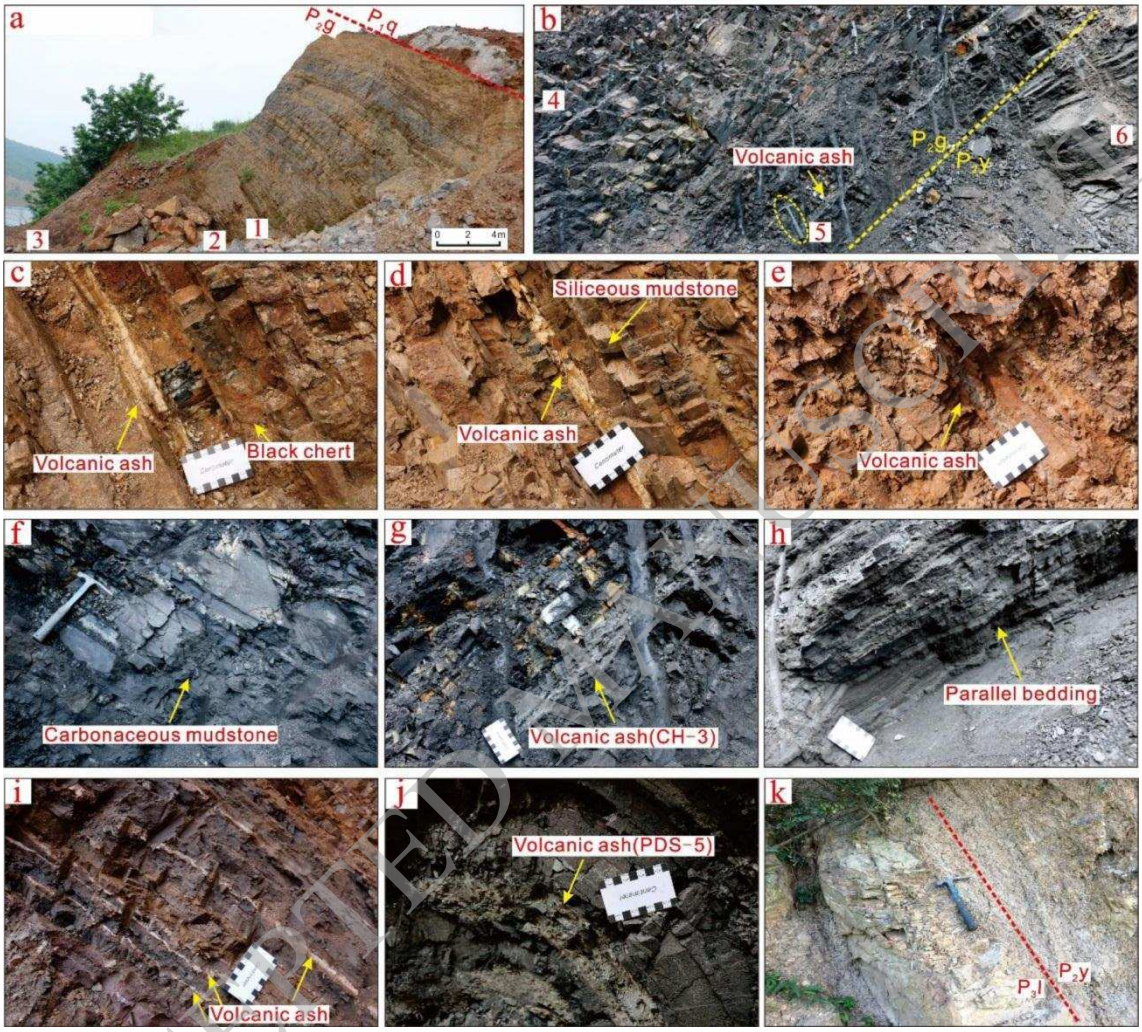

Fig. 4

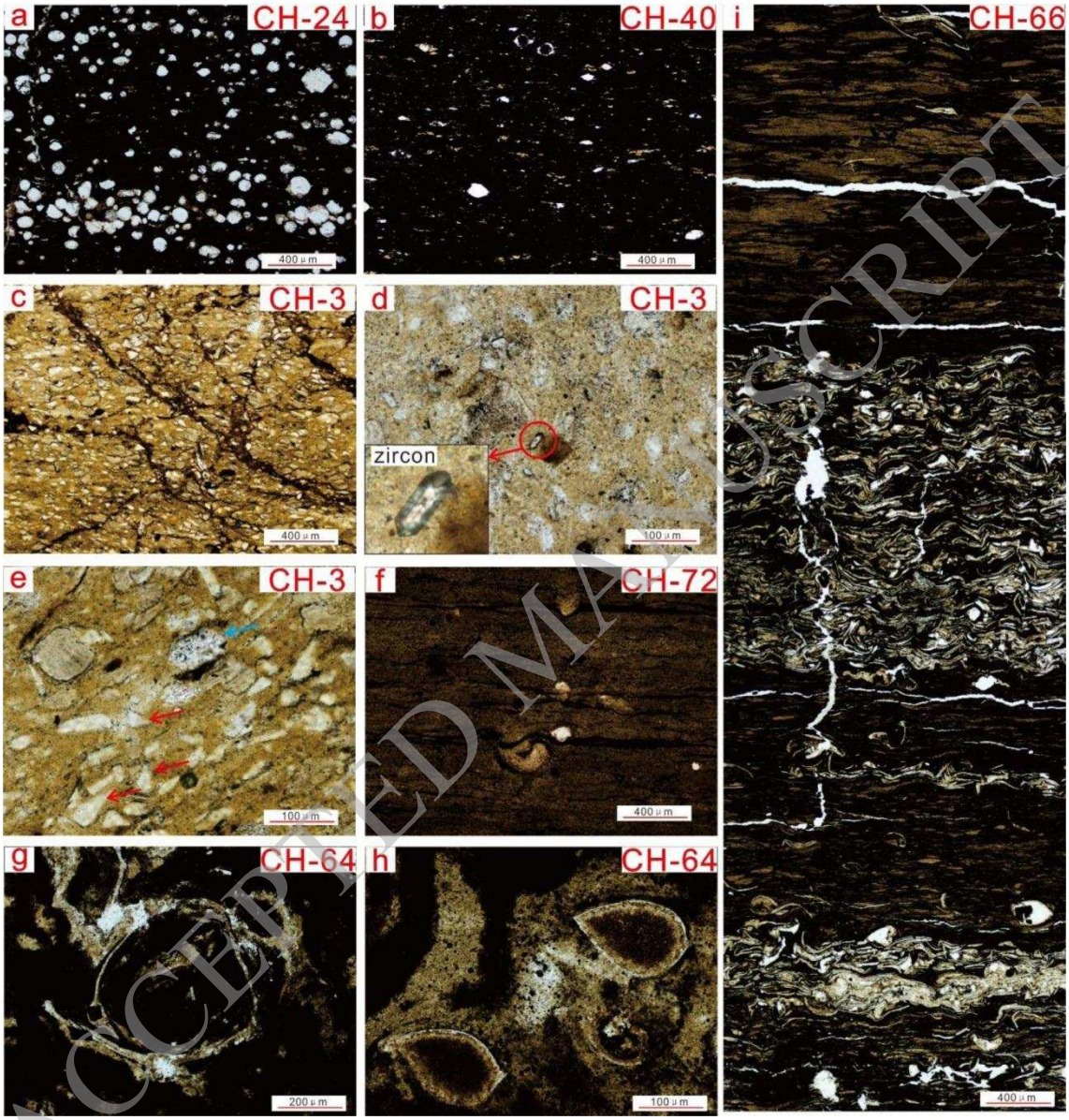

Fig. 5

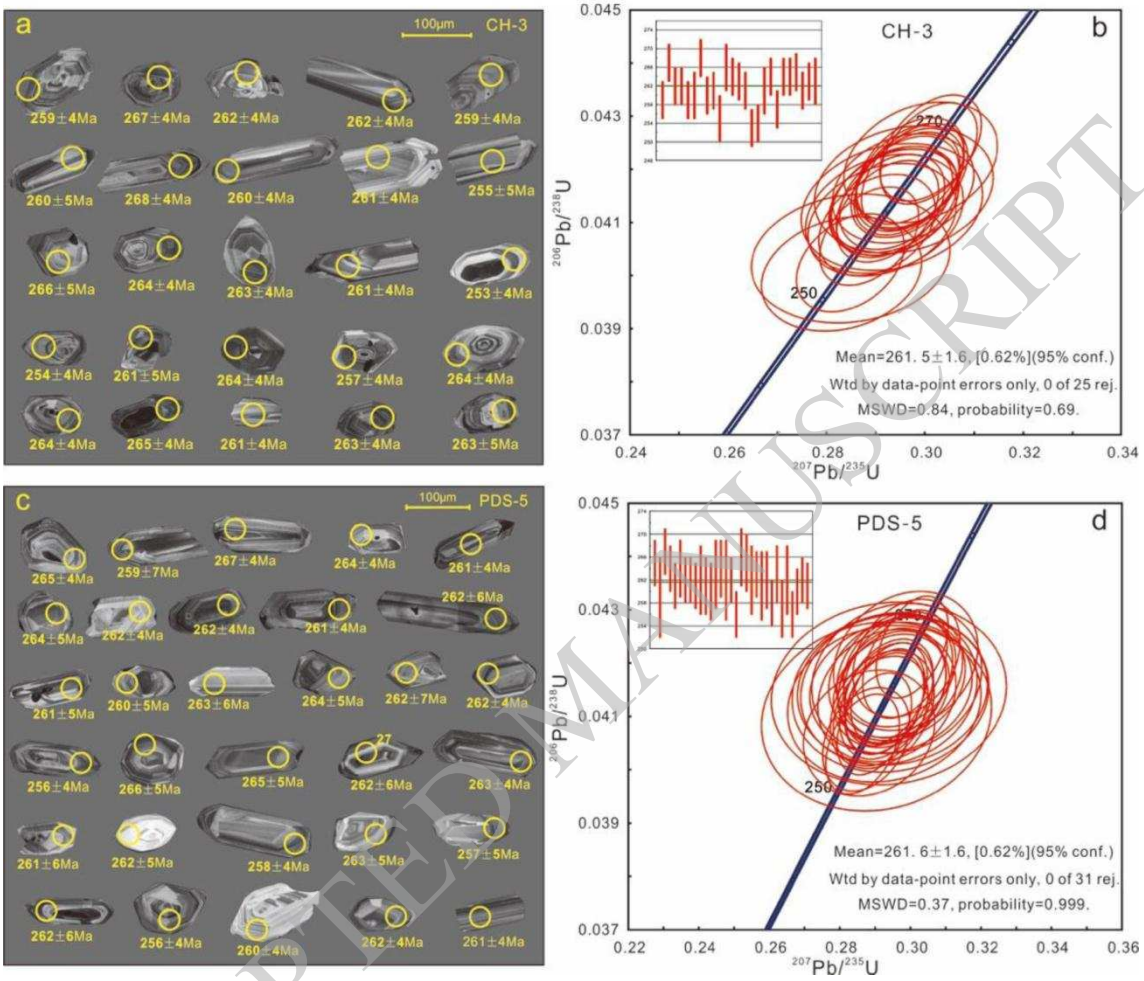

Fig. 6

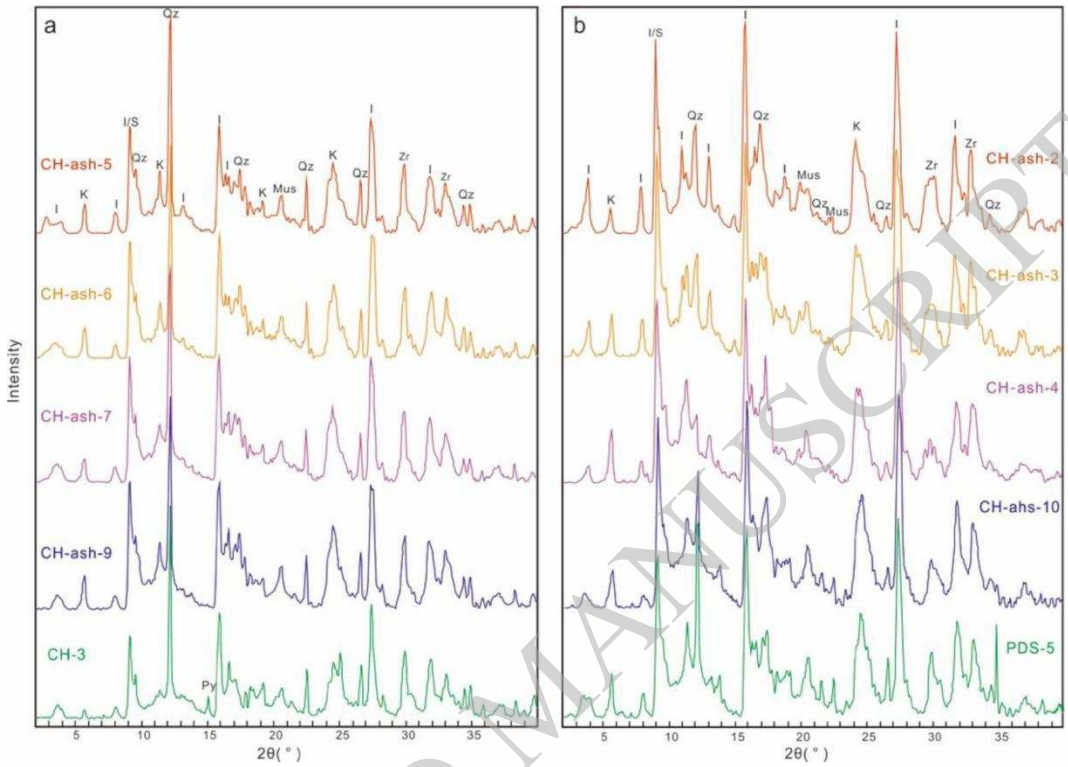

Fig. 7

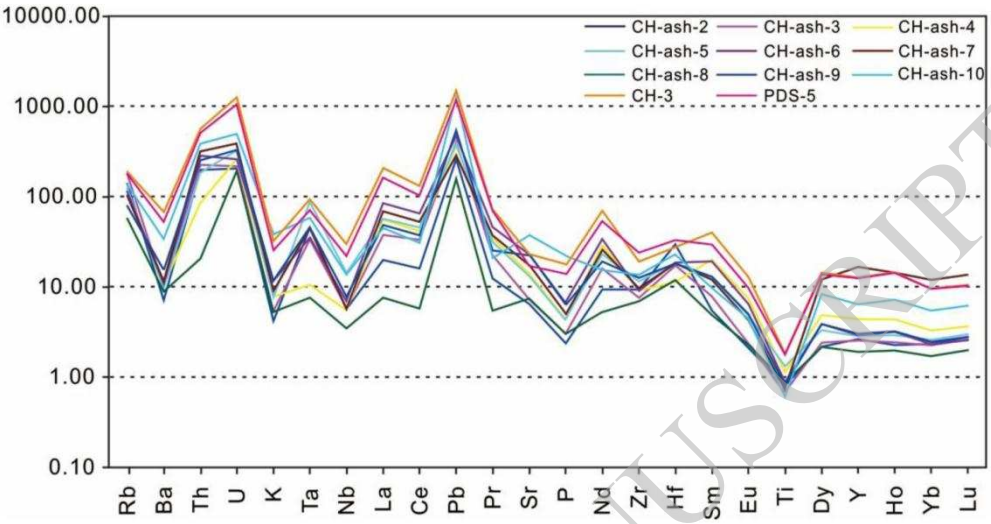

Fig. 8

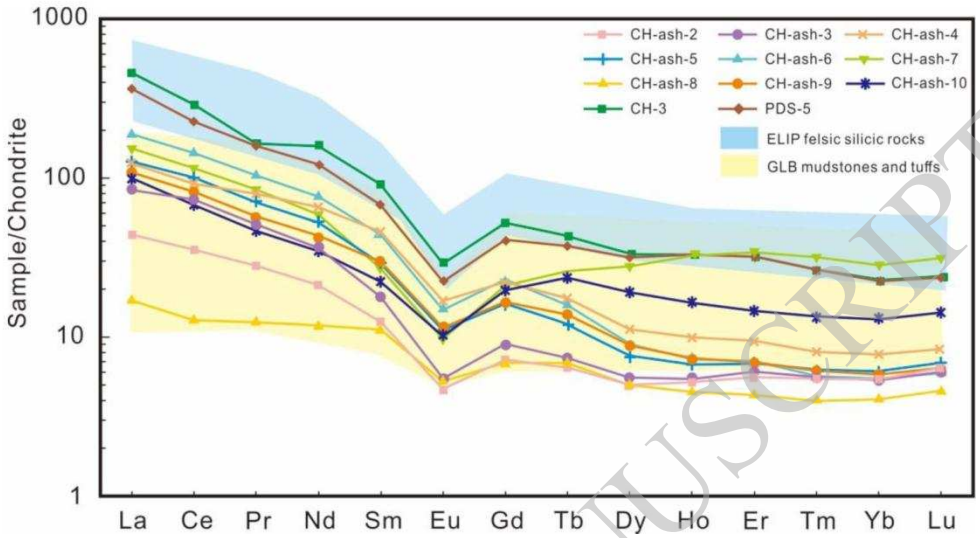

Fig. 9

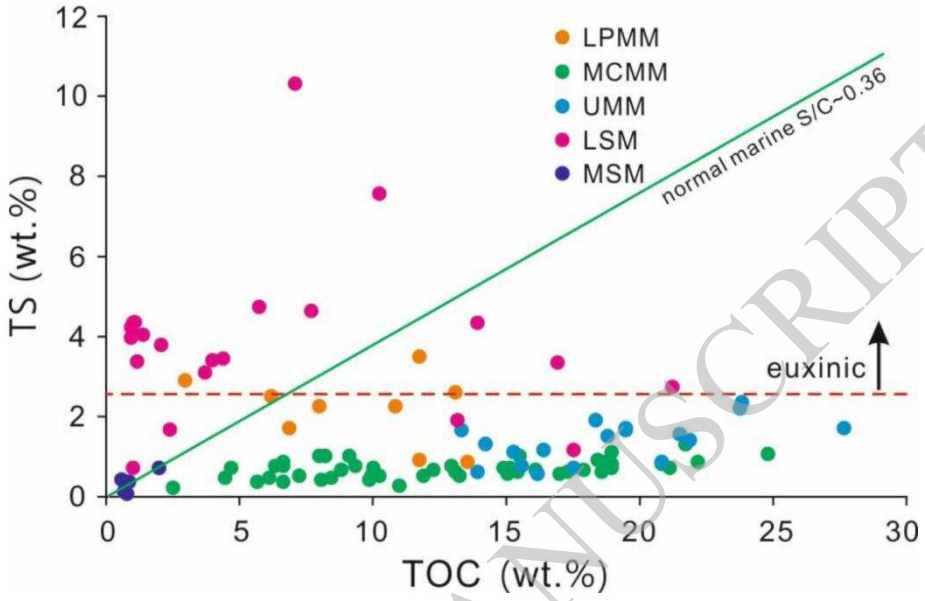

Fig. 10

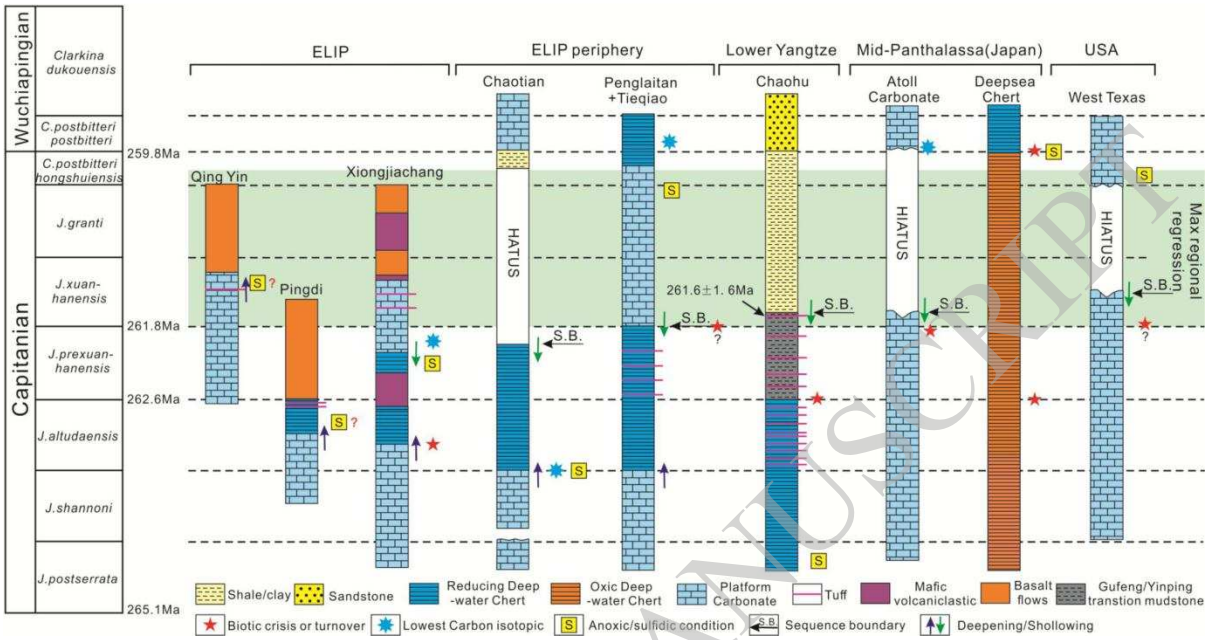

Fig. 11

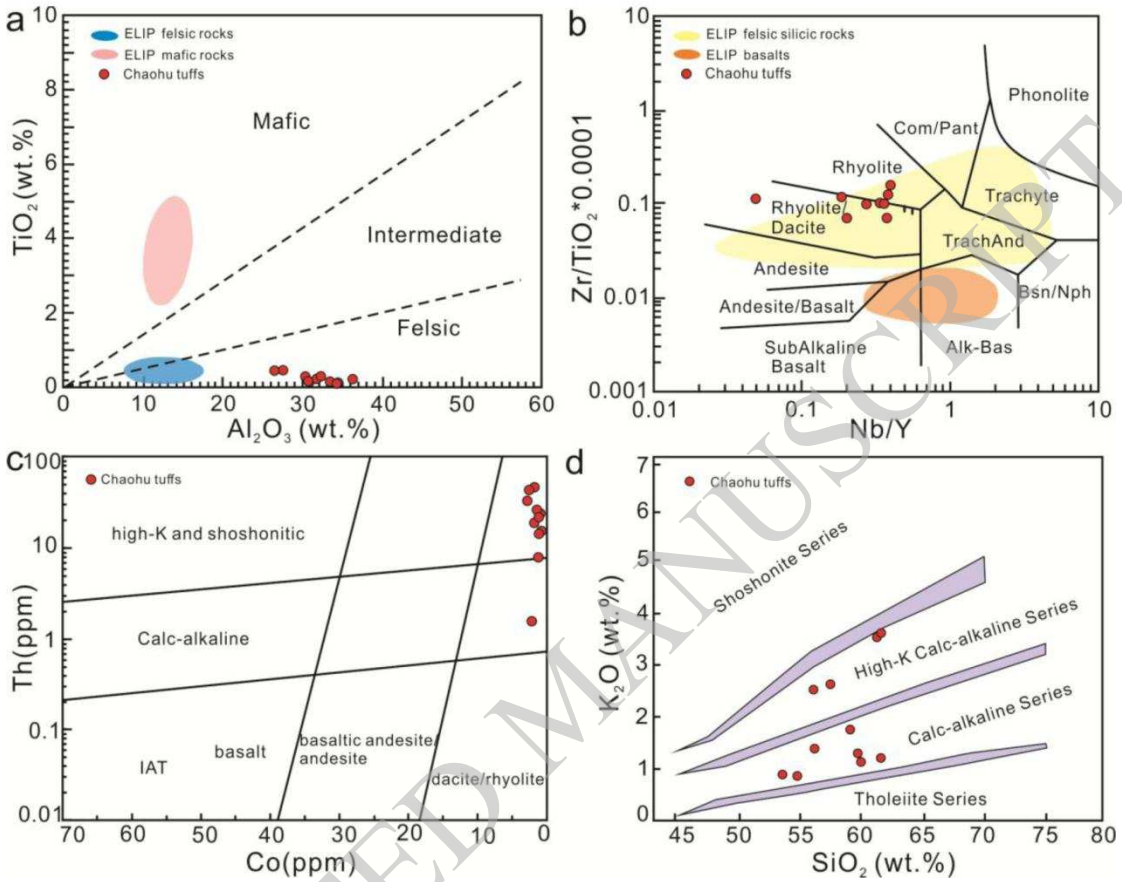

Fig. 12

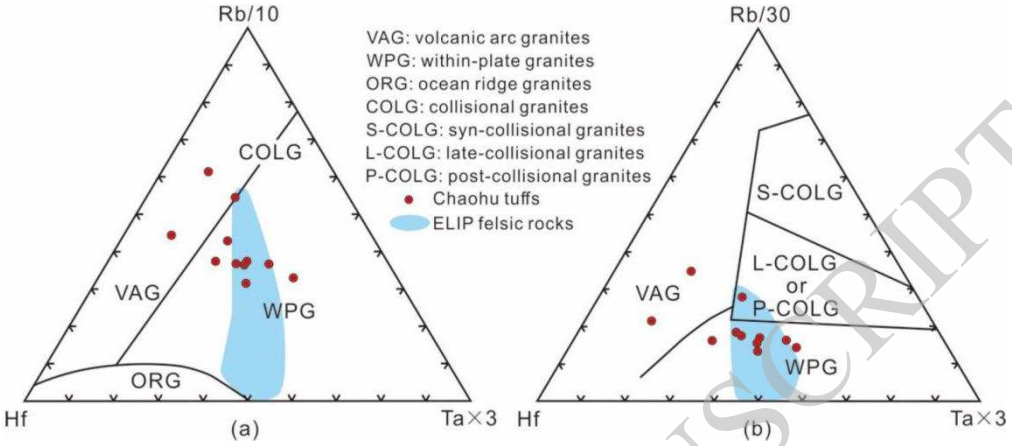

Tables

Table.1 LA-ICP-MS zircon U-Pb dating data from the two tuffs in the Pingdingshan section

Spot	^{232}Th (ppm)	^{238}U (ppm)	^{232}Th/^{238}U	^{207}Pb/^{206}Pb	1σ	^{207}Pb/^{235}U	1σ	^{206}Pb/^{238}U	1σ	^{206}Pb/^{238}U (Ma)	1σ
CH-3-1	139.9	267.7	0.52	0.05142	0.00136	0.29025	0.00782	0.04095	0.00063	259	4
CH-3-2	274.1	420.9	0.65	0.05157	0.00104	0.30079	0.00649	0.0423	0.00063	267	4
CH-3-3	186.7	243.9	0.77	0.05146	0.00128	0.29414	0.00757	0.04146	0.00064	262	4
CH-3-4	152.9	166.0	0.92	0.05144	0.00145	0.2938	0.00847	0.04143	0.00066	262	4
CH-3-5	109.7	175.5	0.63	0.05147	0.00174	0.2913	0.00995	0.04105	0.0007	259	4
CH-3-6	184.7	234.6	0.79	0.05142	0.00186	0.29176	0.01058	0.04116	0.00074	260	5
CH-3-7	263.5	481.3	0.55	0.05151	0.00108	0.30114	0.00681	0.0424	0.00066	268	4
CH-3-8	307.5	351.8	0.87	0.05147	0.00114	0.29242	0.00684	0.04121	0.00063	260	4
CH-3-9	173.0	181.7	0.95	0.05147	0.0015	0.29368	0.00874	0.04138	0.00066	261	4
CH-3-10	364.0	328.0	1.11	0.05126	0.00248	0.28489	0.01332	0.04032	0.0008	255	5
CH-3-11	135.2	252.5	0.54	0.05150	0.00176	0.29914	0.0103	0.04213	0.00075	266	5
CH-3-12	400.6	595.8	0.67	0.05156	0.00112	0.29755	0.00691	0.04186	0.00066	264	4
CH-3-13	180.2	317.1	0.57	0.05149	0.00166	0.29556	0.0095	0.04164	0.00068	263	4
CH-3-14	267.3	362.7	0.74	0.05145	0.00123	0.29299	0.00727	0.04131	0.00064	261	4
CH-3-15	212.9	246.2	0.86	0.05128	0.00197	0.28305	0.01075	0.04003	0.00071	253	4
CH-3-16	148.2	248.4	0.60	0.05135	0.00126	0.28483	0.00722	0.04024	0.00061	254	4
CH-3-17	362.1	399.0	0.91	0.05150	0.00217	0.29328	0.01216	0.04129	0.00079	261	5
CH-3-18	358.2	399.7	0.90	0.05152	0.0012	0.29687	0.00725	0.0418	0.00064	264	4
CH-3-19	313.5	396.4	0.79	0.05140	0.00112	0.28868	0.00665	0.04074	0.00061	257	4
CH-3-20	210.4	383.0	0.55	0.05151	0.00117	0.29635	0.0071	0.04173	0.00064	264	4
CH-3-21	249.1	318.6	0.78	0.05151	0.00124	0.29735	0.00748	0.04188	0.00065	264	4
CH-3-22	301.1	545.1	0.55	0.05134	0.00118	0.29703	0.00722	0.04197	0.00066	265	4
CH-3-23	178.8	193.6	0.92	0.05150	0.0015	0.29381	0.00865	0.04138	0.00066	261	4
CH-3-24	337.4	491.0	0.69	0.05151	0.00122	0.29596	0.00725	0.04167	0.00063	263	4
CH-3-25	169.2	320.9	0.53	0.05153	0.00213	0.29569	0.01199	0.04162	0.00079	263	5
PDS-5-1	253.6	408.3	0.62	0.05157	0.00132	0.29844	0.00791	0.04198	0.00067	265	4
PDS-5-2	463.0	613.7	0.75	0.05134	0.00394	0.29039	0.0215	0.041	0.00117	259	7
PDS-5-3	289.5	424.2	0.68	0.05153	0.00108	0.30051	0.0067	0.0423	0.00063	267	4
PDS-5-4	105.2	147.1	0.72	0.05145	0.00183	0.2969	0.0105	0.04185	0.00069	264	4
PDS-5-5	403.8	382.6	1.06	0.05147	0.00127	0.29261	0.00741	0.04124	0.00063	261	4
PDS-5-6	209.2	291.5	0.72	0.05153	0.00175	0.29654	0.01019	0.04174	0.00075	264	5
PDS-5-7	76.6	123.4	0.62	0.0515	0.0019	0.29455	0.01085	0.04148	0.0007	262	4
PDS-5-8	260.0	367.6	0.71	0.05147	0.00178	0.29478	0.01009	0.04154	0.0007	262	4
PDS-5-9	395.8	604.6	0.65	0.05151	0.0015	0.29323	0.00879	0.04129	0.00072	261	4
PDS-5-10	188.3	290.6	0.65	0.0514	0.00298	0.29393	0.0165	0.04152	0.00094	262	6
PDS-5-11	350.3	385.9	0.91	0.05142	0.00231	0.29333	0.01292	0.04139	0.00082	261	5
PDS-5-12	373.4	352.8	1.06	0.05149	0.00169	0.29202	0.00972	0.04113	0.00073	260	5
PDS-5-13	273.9	256.9	1.07	0.0515	0.00284	0.29615	0.0159	0.04171	0.00093	263	6
PDS-5-14	126.1	222.2	0.57	0.05156	0.00206	0.29698	0.01178	0.04178	0.00078	264	5

PDS-5-15	179.7	289.4	0.62	0.05144	0.00399	0.29391	0.022	0.04143	0.00113	262	7
PDS-5-16	325.2	528.2	0.62	0.05145	0.00121	0.29399	0.00714	0.04144	0.00062	262	4
PDS-5-17	282.0	318.3	0.89	0.05139	0.00144	0.28745	0.00814	0.04057	0.00064	256	4
PDS-5-18	352.1	395.1	0.89	0.05151	0.00171	0.29893	0.01003	0.04209	0.00073	266	5
PDS-5-19	198.0	276.5	0.72	0.05153	0.00235	0.29869	0.01349	0.04204	0.00086	265	5
PDS-5-20	161.6	225.2	0.72	0.05153	0.00334	0.29435	0.01842	0.04144	0.00098	262	6
PDS-5-21	528.5	405.5	1.30	0.05144	0.00179	0.29481	0.0101	0.04158	0.00071	263	4
PDS-5-22	109.9	198.0	0.55	0.05145	0.00327	0.2926	0.01811	0.04124	0.00097	261	6
PDS-5-23	55.7	89.7	0.62	0.05142	0.0027	0.2945	0.01519	0.04154	0.00081	262	5
PDS-5-24	185.1	326.0	0.57	0.05144	0.00117	0.28977	0.00695	0.04086	0.00063	258	4
PDS-5-25	82.2	125.7	0.65	0.05153	0.00226	0.29621	0.01279	0.0417	0.00076	263	5
PDS-5-26	282.1	436.6	0.65	0.0514	0.00224	0.2883	0.01228	0.04069	0.00078	257	5
PDS-5-27	131.8	129.5	1.02	0.05155	0.00323	0.29494	0.01778	0.0415	0.00093	262	6
PDS-5-28	245.2	305.8	0.80	0.05133	0.00118	0.28644	0.00689	0.04048	0.00062	256	4
PDS-5-29	127.9	214.2	0.60	0.05146	0.00154	0.29157	0.00887	0.0411	0.00068	260	4
PDS-5-30	112.4	184.2	0.61	0.05142	0.00142	0.29384	0.00834	0.04145	0.00066	262	4
PDS-5-31	358.2	329.8	1.09	0.05147	0.00125	0.29294	0.00741	0.04128	0.00065	261	4

Table. 2 Major and trace elements of the tuffs in the Pingdingshan section

	CH-ash-2	CH-ash-3	CH-ash-4	CH-ash-5	CH-ash-6	CH-ash-7	CH-ash-8	CH-ash-9	CH-ash-10	CH-3	PDS-5
SiO_2	51.67	49.71	46.84	54.51	53.38	53.4	48.19	53.04	48.96	54.91	53.98
TiO_2	0.183	0.156	0.268	0.306	0.209	0.172	0.206	0.191	0.126	0.41	0.408
Al_2O_3	33.26	34.29	37.42	30.29	31.8	30.92	36.26	30.83	34.02	27.26	26.54
Fe_2O_3	-0.26	0.64	0.37	0.15	0.13	0.49	0.8	1.47	-0.13	1.07	1.78
MnO	-0.004	-0.005	-0.004	-0.004	-0.005	-0.002	-0.005	-0.006	0.002	0.053	0.075
MgO	1.77	1.29	0.65	1.32	1.29	1.52	0.85	1.47	1.19	1.54	1.53
CaO	0.55	0.75	0.61	1	0.87	0.76	0.44	0.57	0.42	0.25	0.22
Na_2O	0.06	0.04	0.11	0.1	0.14	0.12	0.15	0.11	0.18	0.23	0.22
K_2O	1.56	1.21	0.82	1.01	0.95	1.05	0.81	1.14	2.19	3.31	3.19
P_2O_5	0.052	0.067	0.098	0.095	0.146	0.112	0.066	0.145	0.471	0.4	0.315
LOI	11.07	12.72	13.15	10.43	11.11	10.85	13.11	11.28	12.67	9.8	11.05
TOTAL	99.91	100.87	100.33	99.2	100.03	99.39	100.88	100.24	100.1	99.23	99.31
K_2O+Na_2O	1.62	1.25	0.93	1.11	1.09	1.17	0.96	1.25	2.37	3.54	3.41
Al_2O_3/TiO_2	181.75	219.81	139.63	98.99	152.15	179.77	176.02	161.41	270.00	66.49	65.05
Ti	1063.1	876.4	1462.3	1702.7	1132.5	956.5	1134.9	1057.5	792.5	2338.7	2290.4
V	1784.9	1853.4	1731.4	2014.6	1421.1	2325.7	1431.4	1262.3	252.9	216.7	339.6
Ga	38.2	27.4	15.9	23.8	17.5	15.3	10.4	12.2	14.7	24.1	22.1
Rb	88.5	112.5	74.2	78.2	72.1	65.1	36.1	50.2	86.0	119.6	113.4
Sr	136.2	152.9	298.0	277.4	482.0	364.0	156.9	474.6	783.1	488.3	360.5
Y	12.0	11.6	20.0	13.0	13.2	75.8	8.8	13.9	29.2	58.3	57.1
Zr	105.0	85.1	103.5	128.6	101.6	107.8	77.9	140.9	152.3	213.3	268.6
Nb	4.0	4.1	3.9	10.0	5.0	4.0	2.5	5.5	9.7	21.0	15.4
Mo	0.6	1.8	1.4	1.5	1.2	1.1	2.8	3.2	9.9	45.6	41.3
Ba	49.3	69.0	73.3	68.8	76.7	80.1	62.3	107.4	235.1	474.9	362.6
La	13.6	25.9	38.1	39.3	58.5	47.4	5.2	33.6	30.9	142.0	112.5
Ce	28.5	59.1	74.0	81.0	115.8	93.0	10.3	66.1	54.6	233.6	182.6
Pr	3.4	6.2	9.7	8.7	12.6	10.3	1.5	7.0	5.7	20.0	19.4
Nd	12.6	21.7	39.3	31.3	45.7	35.3	7.1	25.9	20.8	95.0	72.8
Sm	2.4	3.5	8.9	5.7	8.6	5.4	2.2	5.8	4.3	17.8	13.2
Eu	0.3	0.4	1.2	0.8	1.1	0.7	0.4	0.8	0.7	2.2	1.6
Gd	1.9	2.3	5.7	4.2	5.9	5.4	1.8	4.4	5.1	13.5	10.6
Tb	0.3	0.3	0.8	0.6	0.8	1.2	0.3	0.7	1.1	2.0	1.8
Dy	1.6	1.8	3.6	2.5	2.9	8.9	1.6	2.9	6.2	10.7	10.2
Ho	0.4	0.4	0.7	0.5	0.5	2.4	0.3	0.5	1.2	2.4	2.3
Er	1.2	1.3	2.0	1.4	1.5	7.2	0.9	1.5	3.1	6.7	6.6
Tm	0.2	0.2	0.3	0.2	0.2	1.0	0.1	0.2	0.4	0.9	0.8
Yb	1.1	1.1	1.6	1.3	1.1	5.9	0.8	1.2	2.7	4.8	4.7
Lu	0.2	0.2	0.3	0.2	0.2	1.0	0.1	0.2	0.5	0.8	0.8
Hf	9.2	5.4	3.5	5.7	5.8	5.6	3.7	5.6	7.1	8.8	10.3
Ta	1.9	1.4	0.4	3.6	1.4	1.9	0.3	1.9	2.4	3.9	2.9
Pb	18.7	28.9	26.0	27.4	33.9	20.6	11.3	38.9	91.3	107.5	84.3

Th	16.8	19.2	7.3	15.7	24.1	27.1	1.7	21.3	32.8	47.8	43.2
U	4.3	4.6	5.6	6.8	5.5	8.3	4.1	7.0	10.5	26.6	22.4
∑REE	79.9	136.1	206.3	190.6	268.6	300.9	41.5	164.6	166.5	610.5	497.1
δEu*	0.5	0.4	0.5	0.5	0.5	0.4	0.6	0.5	0.5	0.4	0.4
δCe*	1.0	1.1	0.9	1.1	1.0	1.0	0.9	1.0	1.0	1.1	0.9
Ti/Th	63.2	45.8	199.9	108.8	46.9	35.2	651.7	49.6	24.1	48.9	53.0
Nb/Ta	2.1	3.0	9.0	2.8	3.4	2.2	7.9	2.9	4.0	5.4	5.3

*$\delta Eu = Eu_N/(Sm_N \times Gd_N)^{1/2}$, $\delta Ce = Ce_N/(La_N \times Pr_N)^{1/2}$, where subscript N denotes chondrite-normalized; normalization values are after Sun and McDonough (1989); ∑REE means total rare earth elements.

Table. 3 The TOC, TS and TS/TOC ratios of the Gufeng and lower-middle Yinping Formation in the Pingdingshan section

Sample	Depth m	Member	TOC wt. %	TS wt. %	TS/TOC	Sample	Depth m	Member	TOC wt. %	TS wt. %	TS/TOC
CSC-1	0.05	LPMM	2.91	2.94	1.01	CH-35	26.35	MCMM	22.11	0.88	0.04
CSC-3	0.25	LPMM	6.13	2.53	0.41	CH-36	26.40	MCMM	10.17	0.54	0.05
CSC-5	0.40	LPMM	7.96	2.26	0.28	CH-37	26.45	MCMM	14.97	0.57	0.04
CSC-7	0.60	LPMM	11.67	0.92	0.08	CH-38	26.60	MCMM	18.50	0.63	0.03
CSC-9	0.90	LPMM	13.49	0.89	0.07	CH-39	26.80	MCMM	6.60	0.42	0.06
CSC-11	1.20	LPMM	13.06	2.65	0.20	CH-40	27.00	MCMM	9.83	0.43	0.04
CSC-13	1.50	LPMM	11.70	3.54	0.30	CH-41	27.10	MCMM	13.20	0.53	0.04
CSC-15	1.90	LPMM	6.83	1.72	0.25	CH-42	27.30	UMM	14.15	1.32	0.09
CSC-17	2.30	LPMM	10.79	2.28	0.21	CH-43	27.50	UMM	13.28	1.71	0.13
CSC-19	2.50	MCMM	9.95	0.75	0.08	CH-44	27.65	UMM	18.31	1.92	0.10
CSC-21	3.20	MCMM	9.29	0.78	0.08	CH-45	27.80	UMM	15.19	1.12	0.07
CSC-24	4.20	MCMM	2.46	0.26	0.11	CH-46	28.00	UMM	19.40	1.70	0.09
CSC-27	5.10	MCMM	6.10	0.48	0.08	CH-47	28.30	UMM	23.66	2.23	0.09
CSC-30	6.00	MCMM	4.46	0.49	0.11	CH-48	28.50	UMM	21.79	1.44	0.07
CSC-33	7.00	MCMM	12.25	0.68	0.06	CH-49	28.65	UMM	23.75	2.39	0.10
CSC-35	8.00	MCMM	13.02	0.64	0.05	CH-50	28.75	UMM	16.32	1.21	0.07
CSC-37	9.00	MCMM	9.94	0.69	0.07	CH-51	28.90	UMM	19.41	1.75	0.09
CSC-40	10.00	MCMM	6.32	0.81	0.13	CH-52	29.10	UMM	18.71	1.53	0.08
CSC-43	10.90	MCMM	4.63	0.73	0.16	CH-53	29.30	UMM	20.73	0.88	0.04
CSC-46	11.70	MCMM	9.06	1.06	0.12	CH-54	29.45	UMM	17.46	0.73	0.04
CSC-49	12.70	MCMM	7.99	1.06	0.13	CH-55	29.70	UMM	15.50	0.77	0.05
CSC-52	13.80	MCMM	7.97	1.04	0.13	CH-56	29.90	UMM	16.11	0.62	0.04
CSC-54	14.60	MCMM	6.60	0.88	0.13	CH-57	30.00	UMM	13.86	0.64	0.05
CSC-56	15.50	MCMM	6.58	0.80	0.12	CH-58	30.20	UMM	21.45	1.60	0.07
CSC-58	16.40	MCMM	8.40	0.51	0.06	CH-59	30.60	UMM	27.56	1.73	0.06
CSC-60	17.30	MCMM	18.90	1.16	0.06	CH-60	30.80	UMM	21.24	2.74	0.13
CSC-62	18.00	MCMM	7.24	0.53	0.07	GS-1	31.00	LSM	17.47	1.19	0.07
CSC-65	18.80	MCMM	15.06	0.74	0.05	CH-62	31.10	LSM	16.86	3.37	0.20
CSC-67	19.60	MCMM	18.93	0.86	0.05	CH-63	31.20	LSM	13.87	4.38	0.32
CSC-68	20.00	MCMM	24.73	1.07	0.04	CH-64	31.30	LSM	3.67	3.12	0.85
CH-1	21.20	MCMM	14.84	0.75	0.05	GS-3	31.40	LSM	2.07	3.82	1.85
CH-3	21.60	MCMM	12.93	0.77	0.06	CH-65	31.50	LSM	5.73	4.78	0.83
CH-7	22.40	MCMM	11.85	0.55	0.05	CH-66	31.60	LSM	7.68	4.68	0.61
CH-9	22.85	MCMM	9.90	0.54	0.05	CH-67	31.70	LSM	4.37	3.46	0.79
CH-10	23.00	MCMM	18.37	0.93	0.05	GS-5	31.85	LSM	13.13	1.94	0.15
CH-14	23.20	MCMM	15.47	1.02	0.07	CH-68	31.90	LSM	7.09	10.31	1.46
CH-17	23.70	MCMM	8.76	0.67	0.08	CH-69	32.00	LSM	10.20	7.58	0.74
CH-19	24.30	MCMM	21.65	1.36	0.06	GS-7	32.10	LSM	3.98	3.41	0.85
CH-21	24.70	MCMM	18.66	0.89	0.05	CH-70	32.20	LSM	1.36	4.08	3.00
CH-23	25.05	MCMM	20.80	0.84	0.04	CH-71	32.40	LSM	0.88	4.25	4.85
CH-24	25.20	MCMM	5.66	0.38	0.07	GS-9	32.50	LSM	1.01	0.75	0.75

CH-25	25.25	MCMM	21.07	0.73	0.03	CH-72	32.70	LSM	0.94	4.02	4.26
CH-26	25.30	MCMM	16.01	0.68	0.04	CH-73	32.90	LSM	1.00	4.35	4.33
CH-27	25.45	MCMM	15.35	0.64	0.04	CH-74	33.20	LSM	1.03	4.35	4.24
CH-28	25.65	MCMM	17.87	0.70	0.04	GS-11	33.40	LSM	2.39	1.68	0.70
CH-29	25.70	MCMM	15.02	0.69	0.05	GS-13	33.80	LSM	1.16	3.38	2.91
CH-30	25.85	MCMM	17.28	0.63	0.04	GS-15	34.40	MSM	0.67	0.13	0.20
CH-31	25.90	MCMM	16.94	0.61	0.04	GS-18	35.30	MSM	0.73	0.11	0.15
CH-32	26.00	MCMM	8.05	0.44	0.05	GS-21	36.10	MSM	1.94	0.75	0.39
CH-33	26.10	MCMM	18.87	0.76	0.04	GS-25	37.50	MSM	0.58	0.43	0.74
CH-34	26.20	MCMM	10.92	0.29	0.03	GS-28	38.50	MSM	0.80	0.38	0.47